

TWO-DIMENSIONAL VISCOUS COMPACTION IN COMPRESSIBLE
GRANULAR MATERIALS

A Thesis

Submitted to the Graduate School
of the University of Notre Dame
in Partial Fulfillment of the Requirements
for the Degree of

Master of Science

by

Michael T. Cochran, B.S.

Joseph M. Powers, Director

Graduate Program in Aerospace and Mechanical Engineering

Notre Dame, Indiana

September 2006

TWO-DIMENSIONAL VISCOUS COMPACTION IN COMPRESSIBLE GRANULAR MATERIALS

Abstract

by

Michael T. Cochran

A set of equations modeling compaction behavior in a two phase mixture of inert granular high explosive and interstitial gas, is discussed and solved numerically in two dimensions. This model treats both phases as compressible, viscous fluids using modified Navier Stokes equations, and standard constitutive relations. One dimensional limits, such as shock tubes and piston-driven problems compare favorably to analytical solutions and experimental data of Sandusky, *et al.*[1], respectively. The model also includes explicit intraphase transfer of mass, momenta, and energy to describe the interactions between the two phases, while at the same time conserving mass, momenta, and energy, and maintaining frame invariance. The equations are then solved using simple two-dimensional extensions of these cases, and the results are compared to the one-dimensional data, with good agreement. Finally, a forcing term, in the form of a concentrated energy source, is used to demonstrate two-dimensional behavior. Compaction is shown to develop in these test problems.

To Elizabeth.

CONTENTS

| | |
|---|------|
| FIGURES | v |
| TABLES | vii |
| SYMBOLS | viii |
| CHAPTER 1: INTRODUCTION | 1 |
| 1.1 Physical System | 1 |
| 1.2 Previous Research | 2 |
| 1.3 Model | 4 |
| 1.4 Scope | 6 |
| CHAPTER 2: GOVERNING EQUATIONS | 8 |
| 2.1 Nearly Conservative Form | 8 |
| 2.2 Non-Conservative Form | 11 |
| 2.3 Constitutive Relations | 12 |
| 2.4 Characteristics | 15 |
| 2.4.1 No Diffusion | 18 |
| 2.4.2 Energy Diffusion | 18 |
| 2.4.3 Momentum and Energy Diffusion | 19 |
| 2.5 Boundary Conditions | 20 |
| CHAPTER 3: NUMERICAL METHOD | 22 |
| 3.1 Equation Forms | 22 |
| 3.2 Numerical Method | 27 |
| 3.3 Meshes and Grid Resolution | 28 |
| CHAPTER 4: VERIFICATION | 29 |
| 4.1 One-Dimensional Shock Tube | 29 |
| 4.2 Convergence and Resolution | 30 |
| 4.2.1 Error Norm | 30 |
| 4.2.2 Shock Thickness | 32 |

| | | |
|---|--------------------------------------|----|
| 4.3 | Piston-Driven Problems | 32 |
| 4.4 | Compaction Wave | 34 |
| 4.5 | Stability | 35 |
| CHAPTER 5: RESULTS | | 39 |
| 5.1 | Two-Dimensional Shock Tube | 39 |
| 5.2 | Two-Dimensional Piston | 43 |
| 5.3 | Forcing Function | 45 |
| 5.4 | Simple Geometry | 47 |
| 5.5 | Long Slender Region | 48 |
| 5.6 | Annulus | 50 |
| CHAPTER 6: DISCUSSION AND FUTURE WORK | | 58 |
| 6.1 | Discussion | 58 |
| 6.2 | Future Work | 59 |
| REFERENCES | | 60 |

FIGURES

| | | |
|-----|---|----|
| 1.1 | Schematic of compaction phenomena induced by a piston | 2 |
| 4.1 | Temperature profiles for shock tube at $t = 60 \mu s$ | 30 |
| 4.2 | Numerical convergence of solid density | 31 |
| 4.3 | Solid volume fraction for a piston at $t = 60 \mu s$ | 35 |
| 4.4 | $x - t$ plot of the wave front for a piston-driven shock | 36 |
| 4.5 | Compaction wave speed versus piston speed showing both numerical and experimental results | 37 |
| 4.6 | Time derivative of gas temperature | 38 |
| 5.1 | Solid temperature for two-dimensional shock tube with periodic bound- ary conditions at $t = 60 \mu s$ | 40 |
| 5.2 | Temperature profiles at the centerline for two-dimensional shock tube at $t = 60 \mu s$ | 41 |
| 5.3 | Solid temperature for two-dimensional shock tube with no-slip bound- ary conditions at $t = 60 \mu s$ | 42 |
| 5.4 | Comparison of gas temperature profiles through the center of the domain for no slip and periodic boundary conditions at $t = 60 \mu s$. . . | 43 |
| 5.5 | Relative difference in solid temperature with and without diffusion of energy and momenta $t = 60 \mu s$ | 44 |
| 5.6 | Gas temperature for the piston-driven problem with periodic bound- ary conditions at $t = 600 \mu s$ | 45 |
| 5.7 | Gas temperature for the piston-driven problem with no-slip boundary conditions at $t = 600 \mu s$ | 46 |
| 5.8 | Initial profile of source term \mathcal{S} | 47 |
| 5.9 | Ideal gas density for a concentrated energy source: higher ratio of specific heats at $t = 60 \mu s$ | 49 |

| | | |
|------|---|----|
| 5.10 | Ideal gas density for a concentrated energy source: lower ratio of specific heats at $t = 60 \mu s$ | 50 |
| 5.11 | Gas density for a concentrated energy source with periodic boundary conditions at $t = 50 \mu s$ | 51 |
| 5.12 | Gas density for a concentrated energy source with periodic boundary conditions at $t = 50 \mu s$ | 52 |
| 5.13 | Gas density for a concentrated heat source with no-slip at $t = 50 \mu s$. | 53 |
| 5.14 | Forcing function, \mathcal{S}_e for the thin annulus | 54 |
| 5.15 | Solid density for a concentrated energy source at $t = 50 \mu s$ | 55 |
| 5.16 | Solid volume fraction for a concentrated energy source at $t = 50 \mu s$. | 56 |
| 5.17 | Kinetic energy for a concentrated energy source at $t = 50 \mu s$ | 57 |

TABLES

2.1 PARAMETER VALUES USED IN THIS STUDY 16

SYMBOLS

| | |
|--------------|--|
| A_{tot} | total area [m^2] |
| a_o | amplitude factor in forcing function [W/m^3] |
| b_g | virial gas coefficient [m^3/kg] |
| b_o | spatial factor in forcing function [m^{-2}] |
| c_v | specific heat at constant volume [$J/kg/K$] |
| e | specific internal energy [J/kg] |
| e_l | local error |
| e_m | mixture energy [J/kg] |
| \mathbf{f} | vector containing the forcing functions |
| \mathbf{G} | vector containing the dependent variables |
| g_i | components of \mathbf{G} |
| H | height of geometric domain [m] |
| \mathbf{I} | unit tensor |
| k | coefficient of thermal conductivity [$W/m/K$] |
| L | length of geometric domain [m] |
| L_c | characteristic length [m] |
| \mathbf{m} | generalized eigenvector |
| N | number of elements |
| p | pressure [Pa] |
| p_m | mixture pressure [Pa] |
| \mathbf{q} | heat flux vector [W/m^3] |

| | |
|-------------------|--|
| \mathbf{q}_m | mixture heat flux vector [W/m^3] |
| T | temperature [K] |
| t | time [s] |
| \mathbf{u} | velocity vector [m/s] |
| u | horizontal component of velocity vector [m/s] |
| v | vertical component of velocity vector [m/s] |
| x | Cartesian space coordinate [m] |
| y | Cartesian space coordinate [m] |
| \mathcal{C} | interphase mass transport rate [$kg/m^3/s$] |
| \mathcal{E} | interphase energy transport rate [W/m^3] |
| \mathcal{F} | source term for material compaction [s^{-1}] |
| \mathcal{H} | coefficient of heat transfer [$W/m^3/K$] |
| \mathcal{M} | interphase transfer of momentum [N/m^3] |
| \mathcal{M}_i | components of interphase transfer of momentum [N/m^3] |
| β_s | configuration stress for the solid [Pa] |
| $\mathbf{\Gamma}$ | matrix containing spatial derivatives of dependent variables |
| γ | ratio of specific heats |
| δ | interphase drag parameter [$kg/m^3/s$] |
| ϵ_s | compaction constant [J/kg] |
| η | entropy [$J/kg/K$] |
| Θ | shock thickness [m] |
| λ | eigenvalue [m/s] |
| μ | coefficient of viscosity [Ns/m^2] |
| μ_c | compaction viscosity [Ns/m^2] |
| ρ | density [kg/m^3] |
| ρ_m | mixture density [kg/m^3] |

| | |
|-----------------------|---|
| ρ_o | initial density [kg/m^3] |
| $\boldsymbol{\tau}$ | viscous stress tensor [Pa] |
| $\boldsymbol{\tau}_m$ | mixture viscous stress tensor [Pa] |
| ϕ | volume fraction |
| ϕ_o | initial volume fraction |
| ψ | Helmholtz free energy [J/kg] |
| $\hat{\psi}_s$ | classical Helmholtz free energy of the solid [J/kg] |

CHAPTER 1

INTRODUCTION

1.1 Physical System

The focus of this study is on two-dimensional continuum mixture models of material which, at the microscale level, is composed of solid grains and gas-filled cavities. The behavior of the material varies markedly from a simple homogeneous solid. The cavities are assumed to make a continuously joined region through which the gas can move. In general, mass, momentum and energy may pass from one phase to the other, though mass transfer is not considered here. The system is insulated, and must globally conserve these quantities, except when a forcing function injects mass, momentum or energy into the system.

It is well known that heterogeneous, porous, energetic, materials can behave in dramatically different ways than do equivalent solid homogeneous energetic materials. Particularly, porous media will show a greater tendency toward detonation with even modest stimuli [2]. These stimuli can come in many forms ranging from physical impact, to injection of energy. In many cases deflagration-to-detonation (DDT) can be triggered by a compaction wave, that is, a wave propagating through the material which causes the solid volume fraction to increase toward unity. Figure 1.1 shows a schematic of compaction induced by a piston driving into the porous material. A compaction wave travels through the ambient porous material, and leaves behind it a region that is almost completely solid. That is, all of the gas phase

has been squeezed into smaller pockets at a higher density, and the solid volume fraction, the ratio of the volume taken up by the solid to that of the total volume of the system, approaches unity. The compaction wave speed U_c is observed to be greater than the piston speed U_p . The porous medium has a significantly increased tendency to detonation. It is not well understood what, exactly, causes this. Some of the plausible explanations suggested by Luebcke, *et al.* [3] are adiabatic shear, intergranular friction, and adiabatic compression of trapped gases, although there is no general consensus on the causes. These phenomena can be particularly problematic in the storage of granular explosive materials, given the relative instability of the granular form as discussed in Gonthier and Powers [2].

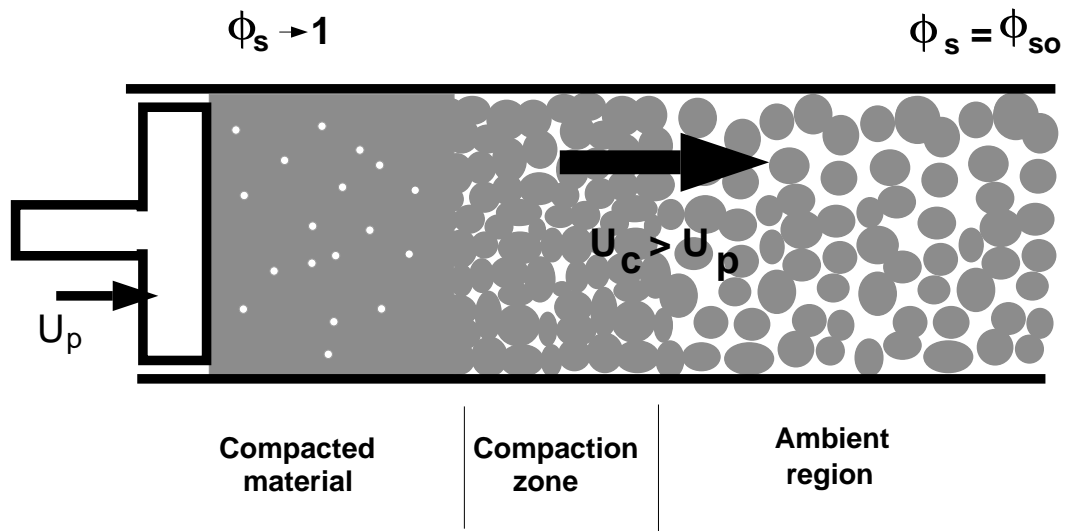


Figure 1.1. Schematic of compaction phenomena induced by a piston

1.2 Previous Research

In a series of studies spearheaded by Sandusky and co-workers in the mid-1980's [4, 1] the behavior of various granular materials was studied in experiments involving

a number of stimuli such as gas-driven and piston-driven compaction. These results have served as benchmarks with which much of the modeling work of subsequent researchers has been compared.

Baer and Nunziato [5] (BN) introduced a general theory for compaction in porous materials that they formulated assuming the continuum theory of mixtures. They drew from the previous work of Krier and Gokhale [6], and Butler, *et al.* [7]. BN has been the basis for much of the current work in the field. Powers, *et al.* [8] use a slightly modified version of BN to study steady state compaction waves in a single phase limit of a porous material. In a series of articles, Powers, *et al.* [9, 10] use a one-dimensional, two-phase model to show that inclusion of compaction work, as done by BN, violates the conservation of energy in the one phase solid limit. Gonthier and Powers [11] solve the full two phase system with a reactive solid, using a correction of the BN model. As well, they show relaxation to steady state for the unsteady one-dimensional problem. In a series of papers by Bdzil, *et al.*[12, 13], hereafter known as BMSKS, the authors further develop the model by making certain reductions, and performing a thorough analysis of various constitutive relations used in the BN model. They offer additional suggestions for improving the BN model. Chinnayya, *et al.* [14] continue the work by investigating the chemistry of reaction, and generalize into two dimensions. Powers [15] expands the BMSKS model by explicitly including diffusion of momenta and energy in one-dimensional chemically inert two phase material. In a different formulation, Papalexandris [16] offers a different model including the spatial gradient of the volume fraction as another independent variable. The predictive value of this model is unclear since no numerical studies have yet been done with this model. Lowe and Greenaway [17] investigate the impact of grain size on compaction phenomena. In particular, they use a simple quadratic approximation for the functional form of the intergranular stress. As with

Papalexandris [16], the predictive power of this formulation is not clear, since the numerical results for the fine grained material have no comparison with experiment, although the prediction for coarser material matches well with Sandusky [1]. Lowe and Longbottom [18] study the effects of grain size, and distribution, on compaction behavior. Much of their work is done using a microscale code that tracks the behavior of each particle in the simulation, whereas most work in this field uses some form of an averaged continuum model. They suggest that the compaction behavior is more dependent on the morphology of the porous bed and on the packing distribution, rather than the size of the individual grains. Gonthier [19] shows that the structure of compaction waves has a dependence on both initial density and on impact strength/speed. The modes of viscoelastic, and viscoplastic deformation are both important in the combustion of granular materials at different densities.

1.3 Model

This study uses BMSKS as its base, with diffusive extensions offered by Powers [15]. BMSKS does a thorough analysis of the BN model and offers some modifications [12].

The BMSKS model describes a region of granular material, with the intergranular pores forming an interconnected region of gas. Ref. [12] develops a set of seven partial differential equations which describe the evolution in both time and space of compaction phenomena. The model assumes a continuum approximation, meaning each phase occupies every point simultaneously. The phase variables are actually local averages that exist over a volume large enough to include enough grains, which are usually on the order of 100 microns in size, and pores, to allow for meaningful averages.

Of particular note, the system formally conserves mass, momenta, and energy of

the entire system, though these quantities can freely pass between the two phases. The BMSKS equation set has been formulated to assure the system is hyperbolic.

The major advantages of BMSKS is the thorough analysis of the second law of thermodynamics, and consequent assurance of it, and its use of thermodynamically consistent equations of state for the solid with an explicit dependence on volume fraction.

BMSKS is a general formulation of the equation set. Following the choices of Powers [15], the following parameters, using the nomenclature of BMSKS, have been assigned these values for this study: $w = 1, b = 0, v = 1, f = 1, a = 0$, and $\alpha = 0$. These choices assure second law satisfaction, Galilean frame invariance, assign dissipation from interphase drag to the gas, assign all compaction work to the solid, assign all energy from reaction to the gas, and ignore dissipation from interphase mass transport.

Since BMSKS does not require the phases to be in pressure equilibrium, but instead relates pressures through a dynamic compaction equation, it also introduces a fundamental asymmetry. This in turn introduces a so-called nozzling term into the system in order to satisfy the second law of thermodynamics, and meet the requirements of a plausible, but *ad hoc*, physical argument given in BMSKS. A consequence of this is that there is no way to cast the system into fully conservative form.

Powers [15] systematically builds on a suggestion of BMSKS [13], that a straightforward way to solve the equations, without relying on complicated numerical methods, is to include simple diffusion to simulate grain-scale physics. In the study presented by this paper, the problem of diffusion has been addressed by including Fourier heat transfer and assuming the phases behave as Newtonian fluids. This accounts for diffusion of momentum and energy in both phases. This has the added

benefit of providing a minimum length scale, independent of the grain size, for physical phenomena. Powers [15] does this by systematically introducing the modes of diffusion. He selects the values for the diffusion coefficients, to assure the length scales to be sufficiently large to include a number of grains. The values chosen are significantly higher than those which are generally encountered in the literature for single phase materials. The use of explicitly formulated diffusion, as well, eliminates the necessity to rely on numerical diffusion to smear numerical noise in the vicinity of shocks and other discontinuities. The major disadvantage of numerical diffusion is that it is reliant on both grid sizes, and the particular numerical technique chosen. Physical diffusion, however, is independent of both method, and grid refinements.

Aside from the explicit inclusion of diffusion, this model differs from BMSKS in two other important ways. First, the equations are cast in general three-dimensional form, although this study focuses on geometries in one and two dimensions. Second, the equations of state are relatively simple, and are thermodynamically consistent, while at the same time having sufficient non-linearity to capture behavior observed in experiment. The constitutive models chosen are in no way unique; any such equations which satisfy frame invariance, material indifference, and are a reasonable approximation to experimental data could have been chosen.

1.4 Scope

Much of the past and current research has focused on one-dimensional limits of two-phase materials. This thesis contains a full two-dimensional analysis of the system presented in Powers [15] and investigates a range of geometries as well.

After an introduction of the system of equations, and the development of the numerical method, in Chapters 2 and 3 respectively, the accuracy of the numerical method will be verified in Chapter 4, by comparison to calorically perfect, ideal gas

shock tube results in one dimension, as well as those from a simple piston-driven one-dimensional cylinder. The convergence of the system will also be shown.

The bulk of the examples, found in Chapter 5, will be two-dimensional extensions of the BMSKS proposed by Powers [15]. There will first be examples of simple two-dimensional extensions of shock tubes and piston problems. Then there will be a set of problems with an extra forcing term in the energy equations. This will initiate compaction behavior in the system. There will be investigation of these problems in different geometries, as well.

Finally, there will be a brief discussion of the results in Chapter 6, and mention of areas for future work.

CHAPTER 2

GOVERNING EQUATIONS

2.1 Nearly Conservative Form

The following set of seven equations (and one inequality) is the nearly conservative form of the governing equations for the BMSKS model used in this study:

$$\frac{\partial}{\partial t}(\rho_s \phi_s) + \nabla \cdot (\rho_s \phi_s \mathbf{u}_s) = \mathcal{C}, \quad (2.1)$$

$$\frac{\partial}{\partial t}(\rho_g \phi_g) + \nabla \cdot (\rho_g \phi_g \mathbf{u}_g) = -\mathcal{C}, \quad (2.2)$$

$$\frac{\partial}{\partial t}(\rho_s \phi_s \mathbf{u}_s) + \nabla \cdot (\rho_s \phi_s \mathbf{u}_s \mathbf{u}_s^T + \phi_s (p_s \mathbf{I} - \boldsymbol{\tau}_s)) = \mathcal{M}, \quad (2.3)$$

$$\frac{\partial}{\partial t}(\rho_g \phi_g \mathbf{u}_g) + \nabla \cdot (\rho_g \phi_g \mathbf{u}_g \mathbf{u}_g^T + \phi_g (p_g \mathbf{I} - \boldsymbol{\tau}_g)) = -\mathcal{M}, \quad (2.4)$$

$$\begin{aligned} & \frac{\partial}{\partial t} \left(\rho_s \phi_s \left(e_s + \frac{1}{2} \mathbf{u}_s \mathbf{u}_s^T \right) \right) + \\ \nabla \cdot \left(\rho_s \phi_s \mathbf{u}_s \left(e_s + \frac{1}{2} \mathbf{u}_s \mathbf{u}_s^T \right) + \phi_s \mathbf{u}_s \cdot (p_s \mathbf{I} - \boldsymbol{\tau}_s) + \phi_s \mathbf{q}_s \right) &= \mathcal{E} + \mathcal{S}_e, \end{aligned} \quad (2.5)$$

$$\begin{aligned} & \frac{\partial}{\partial t} \left(\rho_g \phi_g \left(e_g + \frac{1}{2} \mathbf{u}_g \mathbf{u}_g^T \right) \right) + \\ \nabla \cdot \left(\rho_g \phi_g \mathbf{u}_g \left(e_g + \frac{1}{2} \mathbf{u}_g \mathbf{u}_g^T \right) + \phi_g \mathbf{u}_g \cdot (p_g \mathbf{I} - \boldsymbol{\tau}_g) + \phi_g \mathbf{q}_g \right) &= -\mathcal{E} + \mathcal{S}_e, \end{aligned} \quad (2.6)$$

$$\frac{\partial}{\partial t}(\rho_s) + \nabla \cdot (\rho_s \mathbf{u}_s) = -\frac{\rho_s \mathcal{F}}{\phi_s}, \quad (2.7)$$

$$\frac{\partial}{\partial t}(\rho_s \phi_s \eta_s + \rho_g \phi_g \eta_g) + \nabla \cdot (\rho_s \phi_s \mathbf{u}_s \eta_s + \rho_g \phi_g \mathbf{u}_g \eta_g) \geq -\nabla \cdot \left(\frac{\phi_s \mathbf{q}_s}{T_s} + \frac{\phi_g \mathbf{q}_g}{T_g} \right). \quad (2.8)$$

Equations (2.1)–(2.6) describe the evolution of mass, linear momenta, and energy, and are slightly augmented versions of the compressible, viscous, Navier-Stokes equations, as shown later. Equation (2.7) accounts for compaction, that is changes in volume fractions in the materials, and Equation (2.8) is the second law of thermodynamics for the mixture. Scalar quantities found in Equations (2.1–2.8) are ρ, ϕ, p, e, η , and T . These represent intrinsic density, volume fraction, pressure, energy, entropy, and temperature, respectively. The subscripts s and g denote properties of the solid phase and the gas phase, respectively. The vector quantities \mathbf{u} and \mathbf{q} represent the velocity and the heat fluxes, while $\boldsymbol{\tau}$ is the viscous stress tensor for each phase.

The terms \mathcal{C} , \mathcal{M} and \mathcal{E} account for interphase transfer of mass, momentum and energy between the gas and solid phases. The term \mathcal{F} represents a source term for material compaction. Equations (2.5)–(2.6) include an external forcing function, \mathcal{S}_e which provides energy to the system, and is a function of the spatial coordinates.

Equation (2.7) models the compaction within, and between the phases. Though no rigorous basis exists for the form of \mathcal{F} , the form chosen allows for volume fraction evolution due to both mass transfer and stress/pressure disequilibrium. As well, it is useful in assuring that the system is well posed. Later, it will become evident that the system is not formally conservative because the form of \mathcal{M} is such that the system cannot be cast in a fully conservative form.

Regardless of the form chosen for \mathcal{C} , \mathcal{M} and \mathcal{E} , Equations (2.1)–(2.6) are constructed to formally conserve mixture mass, momentum and energy as long as \mathcal{S}_e is set to zero. By making this choice, and defining the following mixture variables (shown by subscript m) and relative velocities (shown by subscript r):

$$\rho_m \equiv \rho_s \phi_s + \rho_g \phi_g, \tag{2.9}$$

$$\mathbf{u}_m \equiv \frac{\rho_s \phi_s \mathbf{u}_s + \rho_g \phi_g \mathbf{u}_g}{\rho_s \phi_s + \rho_g \phi_g}, \quad (2.10)$$

$$\mathbf{u}_{rs} \equiv \mathbf{u}_s - \mathbf{u}_m, \quad (2.11)$$

$$\mathbf{u}_{rg} \equiv \mathbf{u}_g - \mathbf{u}_m, \quad (2.12)$$

$$p_m \equiv \phi_s \left(p_s + \frac{1}{3} \rho_s \mathbf{u}_{rs} \cdot \mathbf{u}_{rs} \right) + \phi_g \left(p_g + \frac{1}{3} \rho_g \mathbf{u}_{rg} \cdot \mathbf{u}_{rg} \right), \quad (2.13)$$

$$e_m \equiv \frac{\rho_s \phi_s \left(e_s + \frac{\mathbf{u}_{rs} \cdot \mathbf{u}_{rs}}{2} \right) + \rho_g \phi_g \left(e_g + \frac{\mathbf{u}_{rg} \cdot \mathbf{u}_{rg}}{2} \right)}{\rho_s \phi_s + \rho_g \phi_g}, \quad (2.14)$$

$$\begin{aligned} \boldsymbol{\tau}_m \equiv & \phi_s \left(\boldsymbol{\tau}_s - \rho_s \left(\mathbf{u}_{rs} \mathbf{u}_{rs}^T - \frac{1}{3} (\mathbf{u}_{rs} \cdot \mathbf{u}_{rs}) \mathbf{I} \right) \right) + \\ & \phi_g \left(\boldsymbol{\tau}_g - \rho_g \left(\mathbf{u}_{rg} \mathbf{u}_{rg}^T - \frac{1}{3} (\mathbf{u}_{rg} \cdot \mathbf{u}_{rg}) \mathbf{I} \right) \right), \end{aligned} \quad (2.15)$$

$$\begin{aligned} \mathbf{q}_m \equiv & \phi_s \left(\rho_s \mathbf{u}_{rs} \left(e_s + \frac{\mathbf{u}_{rs} \cdot \mathbf{u}_{rs}}{2} \right) + \mathbf{u}_{rs} \cdot (p_s \mathbf{I} - \boldsymbol{\tau}_s) + \mathbf{q}_s \right) + \\ & \phi_g \left(\rho_g \mathbf{u}_{rg} \left(e_g + \frac{\mathbf{u}_{rg} \cdot \mathbf{u}_{rg}}{2} \right) + \mathbf{u}_{rg} \cdot (p_g \mathbf{I} - \boldsymbol{\tau}_g) + \mathbf{q}_g \right), \end{aligned} \quad (2.16)$$

it is a straightforward process to show that summing the individual mass, momentum and energy equations, and substituting Equations (2.9)–(2.16) into Equations (2.1)–(2.6) yields the following set of equations:

$$\frac{\partial}{\partial t}(\rho_m) + \nabla \cdot (\rho_m \mathbf{u}_m) = 0, \quad (2.17)$$

$$\frac{\partial}{\partial t}(\rho_m \mathbf{u}_m) + \nabla \cdot (\rho_m \mathbf{u}_m \mathbf{u}_m^T + p_m \mathbf{I} - \boldsymbol{\tau}_m) = 0, \quad (2.18)$$

$$\begin{aligned} & \frac{\partial}{\partial t} \left(\rho_m \left(e_m + \frac{\mathbf{u}_m \cdot \mathbf{u}_m}{2} \right) \right) + \\ \nabla \cdot \left(\rho_m \mathbf{u}_m \left(e_m + \frac{\mathbf{u}_m \cdot \mathbf{u}_m}{2} \right) + \mathbf{u}_m \cdot (p_m \mathbf{I} - \boldsymbol{\tau}_m) + \mathbf{q}_m \right) & = 0. \end{aligned} \quad (2.19)$$

These are the classical compressible Navier-Stokes equations for fluid flow.

The form of \mathcal{M} is such that the equations cannot be cast in a fully conservative system. The forms chosen for \mathcal{C} , \mathcal{M} , \mathcal{E} and \mathcal{F} are given by BMSKS as:

$$\mathcal{C} = \mathcal{C}(\rho_s, \rho_g, T_s, T_g, \phi_s), \quad (2.20)$$

$$\mathcal{M} = p_g \nabla \phi_s - \delta(\mathbf{u}_s - \mathbf{u}_g) + \frac{1}{2}(\mathbf{u}_s - \mathbf{u}_g)\mathcal{C}, \quad (2.21)$$

$$\mathcal{E} = \mathcal{H}(T_g - T_s) - p_g \mathcal{F} + \mathbf{u}_s \cdot \mathcal{M} + \left(e_s - \frac{\mathbf{u}_s \cdot \mathbf{u}_s}{2} \right) \mathcal{C}, \quad (2.22)$$

$$\mathcal{F} = \frac{\phi_s \phi_g}{\mu_x} (p_s - \beta_s - p_g). \quad (2.23)$$

Equations (2.20)–(2.23) are specified by BMSKS as the transport equations for interphase phenomena, chosen to assure frame invariance and to satisfy the second law. Since this study deals only with chemically inert materials, the term \mathcal{C} is set to zero.

Equation (2.21) contains a gradient operator, $p_g \nabla \phi$ in the first term. Elsewhere, all terms to which the gradient operator is applied remain on the left hand side of Equations (2.1)–(2.6). This means that Equations (2.1)–(2.7) are not formally conservative. Computationally, this does not cause any problems for the viscous system considered here. For inviscid counterparts, computational issues remain as discussed by BMSKS [12] and others.

2.2 Non-Conservative Form

For the model used, it is necessary that the entire volume be filled with either gas or solid. There are no voids, nor are there any non-interacting portions of the volume,

$$\phi_s + \phi_g = 1. \quad (2.24)$$

Consequently,

$$\frac{\partial \phi_s}{\partial t} = -\frac{\partial \phi_g}{\partial t} \quad \text{and} \quad \nabla \phi_s = -\nabla \phi_g. \quad (2.25)$$

By successively eliminating terms of mass from the momentum and energy equations, eliminating momentum terms from the energy equations, and directly invoking

ing the interphase transport equations (Equations (2.20)–(2.23)), as well as invoking Equation (2.25), it is possible to cast the system into a fully nonconservative form. Here, $d/dt_s \equiv \partial/\partial t + \mathbf{u}_s \cdot \nabla$, and $d/dt_g \equiv \partial/\partial t + \mathbf{u}_g \cdot \nabla$:

$$\frac{d\rho_s}{dt_s} = -\rho_s \nabla \cdot \mathbf{u}_s - \frac{\rho_s \mathcal{F}}{\phi_s}, \quad (2.26)$$

$$\frac{d\rho_g}{dt_g} = -\rho_g \nabla \cdot \mathbf{u}_g + \frac{\rho_g \mathcal{F}}{\phi_g} + \frac{\mathcal{C}}{\phi_g} \left(\frac{\rho_g}{\rho_s} - 1 \right) + \frac{\rho_g}{\phi_g} (\mathbf{u}_s - \mathbf{u}_g) \cdot \nabla \phi_g, \quad (2.27)$$

$$\begin{aligned} \rho_s \phi_s \frac{d\mathbf{u}_s}{dt_s} &= -\phi_s \nabla p_s + \phi_s \nabla \cdot \boldsymbol{\tau}_s + \boldsymbol{\tau}_s \cdot \phi_s - \delta(\mathbf{u}_s - \mathbf{u}_g) + \frac{1}{2}(\mathbf{u}_g - \mathbf{u}_s) \mathcal{C} + \\ &\quad (p_g - p_s) \nabla \phi_s \end{aligned} \quad (2.28)$$

$$\rho_g \phi_g \frac{d\mathbf{u}_g}{dt_g} = -\phi_g \nabla p_g + \phi_g \nabla \cdot \boldsymbol{\tau}_g + \boldsymbol{\tau}_g \cdot \phi_g + \delta(\mathbf{u}_s - \mathbf{u}_g) + \frac{1}{2}(\mathbf{u}_g - \mathbf{u}_s) \mathcal{C}, \quad (2.29)$$

$$\begin{aligned} \rho_s \phi_s \frac{de_s}{dt_s} &= -p_s \phi_s \nabla \cdot \mathbf{u}_s + \phi_s \boldsymbol{\tau}_s : \nabla \mathbf{u}_s - p_s \mathcal{F} + \mathcal{H}(T_g - T_s) - \\ &\quad \phi_s \nabla \cdot \mathbf{q}_s - \mathbf{q}_s \cdot \nabla \phi_s, \end{aligned} \quad (2.30)$$

$$\begin{aligned} \rho_g \phi_g \frac{de_g}{dt_g} &= -p_g \phi_g \nabla \cdot \mathbf{u}_g + \phi_g \boldsymbol{\tau}_g : \nabla \mathbf{u}_g - p_g \mathcal{F} + \mathcal{H}(T_g - T_s) - \\ &\quad \phi_g \nabla \cdot \mathbf{q}_g - \mathbf{q}_g \cdot \nabla \phi_g + \\ &\quad \delta(\mathbf{u}_s - \mathbf{u}_g) \cdot (\mathbf{u}_s - \mathbf{u}_g) - (e_s - e_g) \mathcal{C} + p_g (\mathbf{u}_s - \mathbf{u}_g), \end{aligned} \quad (2.31)$$

$$\frac{d\phi_s}{dt_s} = \mathcal{F} + \frac{\mathcal{C}}{\rho_s}. \quad (2.32)$$

2.3 Constitutive Relations

Closure of the system, Equations (2.1)–(2.7), requires specifying a certain number of constitutive (non-axiomatic) equations as follows:

$$p_s = \rho_s^2 \left. \frac{\partial \psi_s}{\partial \rho_s} \right|_{T_s, \phi_s}, \quad (2.33)$$

$$p_g = \rho_g^2 \left. \frac{\partial \psi_g}{\partial \rho_g} \right|_{T_g}, \quad (2.34)$$

$$\eta_s = - \left. \frac{\partial \psi_s}{\partial T_s} \right|_{\rho_s, \phi_s}, \quad (2.35)$$

$$\eta_g = -\left.\frac{\partial\psi_g}{\partial T_g}\right|_{\rho_g}, \quad (2.36)$$

$$e_s = \psi_s + T_s\eta_s, \quad (2.37)$$

$$e_g = \psi_g + T_g\eta_g, \quad (2.38)$$

$$\beta_s = \left.\rho_s\phi_s\frac{\partial\psi_s}{\partial\phi_s}\right|_{\rho_s,T_s}, \quad (2.39)$$

$$\psi_s = \hat{\psi}(\rho_s, T_s) + B(\phi_s), \quad (2.40)$$

$$\psi_g = \psi_g(\rho_g, T_g), \quad (2.41)$$

$$\boldsymbol{\tau}_s = 2\mu_s \left(\frac{(\nabla\mathbf{u}_s)^T + \nabla\mathbf{u}_s}{2} - \frac{1}{3}(\nabla\cdot\mathbf{u}_s)\mathbf{I} \right), \quad (2.42)$$

$$\boldsymbol{\tau}_g = 2\mu_g \left(\frac{(\nabla\mathbf{u}_g)^T + \nabla\mathbf{u}_g}{2} - \frac{1}{3}(\nabla\cdot\mathbf{u}_g)\mathbf{I} \right), \quad (2.43)$$

$$\mathbf{q}_s = -k_s\nabla T_s, \quad (2.44)$$

$$\mathbf{q}_g = -k_g\nabla T_g. \quad (2.45)$$

The following new parameters appear in Equations (2.33)–(2.45): coefficient of viscosity, μ ; the compaction viscosity, μ_c ; coefficient of thermal conductivity, k ; interphase drag parameter, δ ; and interphase heat transfer coefficient, \mathcal{H} . In this study, all of these values are considered constants, but the model does not necessarily require this restriction; any or all of these parameters could have a dependence on the state of the system. Helmholtz free energy, ψ , and the configuration stress for the solid, β_s , are new variables to the system.

Equations (2.33)–(2.38) are definitions of canonical thermodynamic relationships for pressure, energy, and entropy. Equations (2.42)–(2.43) are statements of the standard Newtonian relations between viscous stresses and strain rate for isotropic compressible fluids which satisfy Stokes' assumption. Equations (2.44)–(2.45) state Fourier's law of heat transfer. Equations (2.40)–(2.41) are classical (as yet unspecified) equations of state for the solid and gas. The free energy associated with configurational stresses appears as the new variable $B(\phi)$, and Equation (2.39) is

the definition given by BMSKS for the configurational stress.

Though the equations of state (Equations (2.40)–(2.41)) are in general terms, it is necessary to define specific forms for numerical studies. This study, following Powers [15], employs a standard virial equation of state for the gas of the following form:

$$\psi_g(\rho_g, T_g) = c_{vg}T_g \left(1 - \ln \left(\frac{T_g}{T_{go}} \right) + (\gamma_g - 1) \left(\ln \left(\frac{\rho_g}{\rho_{go}} \right) + b_g(\rho_g - \rho_{go}) \right) \right). \quad (2.46)$$

In Equation (2.46), c_{vg} is the constant specific heat at constant volume for the gas; b_g is the virial coefficient; γ_g is the ratio of specific heats for the gas; and ρ_{go} and T_{go} are the initial, reference, states for the system.

Using Equation (2.46) with Equation (2.34), Equation (2.36) and Equation (2.38) yields the following forms for gas pressure, gas entropy and energy:

$$p_g = (\gamma_g - 1)c_{vg}\rho_g T_g(1 + b_g\rho_g), \quad (2.47)$$

$$\eta_g = c_{vg} \left(\ln \left(\frac{T_g}{T_{go}} \right) - (\gamma_g - 1) \left(\ln \left(\frac{\rho_g}{\rho_{go}} \right) + b_g(\rho_g - \rho_{go}) \right) \right), \quad (2.48)$$

$$e_g = c_{vg}T_g. \quad (2.49)$$

The case of the solid is slightly more complicated. Powers [15] uses a modified Tait equation to account for compaction. The form was stated incorrectly; Schwendeman [20], however, offers a corrected form which gives the following for ψ_s :

$$\begin{aligned} \psi_s(\rho_s, T_s, \phi_s) = c_{vs}T_s \left(1 - \ln \left(\frac{T_s}{T_{so}} \right) + (\gamma_s - 1) \ln \left(\frac{\rho_s}{\rho_{so}} \right) \right) + \frac{\epsilon_s \rho_{so}}{\gamma_s \rho_s} + q \\ + \frac{(p_{so} - p_{go})(2 - \phi_{so})^2}{\rho_{so} \phi_{so} \ln \left(\frac{1}{1 - \phi_{so}} \right)} \ln \left(\left(\frac{2 - \phi_{so}}{2 - \phi_s} \right) \frac{(1 - \phi_s)^{\frac{1 - \phi_s}{2 - \phi_s}}}{(1 - \phi_{so})^{\frac{1 - \phi_{so}}{2 - \phi_{so}}}} \right). \end{aligned} \quad (2.50)$$

As with the gas, c_{vs} and γ_s represent the constant of specific heat at constant volume, and the ratio of specific heats of the solid. The constants $\rho_{so}, T_{so}, \phi_{so}, p_{so}$ and p_{go} are the initial states of solid density, solid temperature, solid volume fraction, solid pressure and gas pressure respectively. The remaining parameters are ϵ_s , which is a factor used to match experimental data, and q , which is the chemical energy of the solid. In this study, q is always equal to zero. Applying Equation (2.50) to Equation (2.33), Equation (2.35), Equation (2.37) and Equation (2.39) gives the following forms for solid pressure, entropy and energy and solid configuration stress:

$$p_s = (\gamma_s - 1)c_{vs}\rho_s T_s - \frac{1}{\gamma_s}\rho_{so}\epsilon_s, \quad (2.51)$$

$$\eta_s = c_{vs} \left(\ln \left(\frac{T_s}{T_{so}} \right) - (\gamma_s - 1) \ln \left(\frac{\rho_s}{\rho_{so}} \right) \right), \quad (2.52)$$

$$e_s = c_{vs}T_s + \frac{\epsilon_s\rho_{so}}{\gamma_s\rho_s} + q + \frac{(p_{so} - p_{go})(2 - \phi_{so})^2}{\rho_{so}\phi_{so}\ln\left(\frac{1}{1-\phi_{so}}\right)} \ln \left(\left(\frac{2 - \phi_{so}}{2 - \phi_s} \right) \frac{(1 - \phi_s)^{\frac{1-\phi_s}{2-\phi_s}}}{(1 - \phi_{so})^{\frac{1-\phi_{so}}{2-\phi_{so}}}} \right), \quad (2.53)$$

$$\beta_s = (p_{so} - p_{go}) \frac{\rho_s\phi_s}{\rho_{so}\phi_{so}} \left(\frac{2 - \phi_{so}}{2 - \phi_s} \right)^2 \frac{\ln\left(\frac{1}{1-\phi_s}\right)}{\ln\left(\frac{1}{1-\phi_{so}}\right)}. \quad (2.54)$$

Table 2.1 reports the values for all of the parameters in the governing and constitutive Equations (2.1)–(2.54).

2.4 Characteristics

In order to find necessary boundary and initial conditions for a well posed problem, it is necessary to perform a characteristic analysis of the system. The method described here, closely follows the discussion and results of Powers [15]. The limit of a one-dimensional system leads to greatly simplified analysis, and will be done here.

TABLE 2.1

PARAMETER VALUES USED IN THIS STUDY

| Parameter | Units | Value |
|-------------------|------------|---|
| μ_g | Ns/m^2 | 1.0×10^0 |
| μ_s | Ns/m^2 | 1.0×10^3 |
| k_g | $W/m/K$ | 1.0×10^3 |
| k_s | $W/m/K$ | 1.0×10^0 |
| γ_g | -- | 2.7×10^0 1.35×10^0 |
| γ_s | -- | 5.0×10^0 |
| c_{vg} | $J/kg/K$ | 2.4×10^3 |
| c_{vs} | $J/kg/K$ | 1.5×10^3 |
| T_{go} | K | 3.0×10^2 |
| T_{so} | K | 3.0×10^2 |
| ρ_{go} | kg/m^3 | 1.0×10^0 |
| ρ_{so} | kg/m^3 | 1.9×10^3 |
| $\hat{\rho}_{go}$ | kg/m^3 | 1.1×10^0 |
| $\hat{\rho}_{so}$ | kg/m^3 | 2.0×10^3 |
| ϕ_{so} | -- | 7.3×10^{-1} |
| μ_c | Ns/m^2 | 1.0×10^3 |
| δ | $kg/m^3/s$ | 1.0×10^8 |
| \mathcal{H} | $W/m^3/K$ | 1.0×10^{10} |
| \mathcal{C} | $kg/m^3/s$ | 0 |
| q | J/kg | 0 |
| b_g | m^3/kg | 1.1×10^{-3} |
| ϵ_s | J/kg | 8.98×10^6 |
| a_o | W/m^3 | 1×10^{14} |
| b_o | m^{-2} | 1×10^6 |

In one dimension, the system Equations (2.1)–(2.7) (using appropriate constitutive relations, Equations (2.33)–(2.45)) can be cast in the form:

$$\mathbf{A} \cdot \frac{\partial \mathbf{w}}{\partial t} + \mathbf{B} \cdot \frac{\partial \mathbf{w}}{\partial x} = \mathbf{c}. \quad (2.55)$$

Here, \mathbf{w} is an $n \times 1$ vector of dependent variables, \mathbf{c} is also an $n \times 1$ vector representing the right hand sides of Equations (2.1)–(2.7). Finally, \mathbf{A} and \mathbf{B} are $n \times n$ vectors which are functions of x , t , and \mathbf{w} .

Following the standard method of Zauderer [21], one must find curves in $x - t$ space such that $dx/dt = \lambda$, along which Equation (2.55) becomes a set of ordinary differential equations. To do so, it is necessary to solve a generalized eigenvalue problem:

$$\mathbf{m} \cdot (\lambda \mathbf{A} - \mathbf{B}) = \mathbf{0}, \quad (2.56)$$

where \mathbf{m} and λ are generalized eigenvectors and generalized eigenvalues respectively. Since \mathbf{m} is a general, non-zero, vector, Equation (2.56) is only satisfied if

$$|\lambda \mathbf{A} - \mathbf{B}| = 0. \quad (2.57)$$

If all generalized eigenvalues are real, and n linearly independent generalized eigenvectors exist, then the system is hyperbolic. If there is a lack of linearly independent generalized eigenvectors, but the generalized eigenvalues are still real, then the system is parabolic. An elliptic system is one for which all of the generalized eigenvalues are complex. Although it is not easy to formulate problems which are well posed in the sense of Hadamard, generally, hyperbolic systems are well posed provided that initial conditions exist on a curve that is not a characteristic for the system. Parabolic systems require a mixture of initial and boundary conditions, and

elliptic systems do not generally evolve in time, so require boundary conditions on all geometric boundaries.

2.4.1 No Diffusion

For the case of an inviscid thermally insulated system, that is $k_s = k_g = \mu_s = \mu_g = 0$, it is well known that the system of Equations (2.1)–(2.7) is hyperbolic. Baer and Nunziato [5] show that the dimension for this system is $n = 7$, from which:

$$\lambda = u_s, u_s, u_s \pm c_s, u_g, u_g \pm c_g. \quad (2.58)$$

Here, the isentropic sound speeds of the solid and gas, c_s and c_g respectively, are introduced as:

$$c_s = \sqrt{\left. \frac{\partial p_s}{\partial \rho_s} \right|_{\eta_s, \phi_s}}, \quad c_g = \sqrt{\left. \frac{\partial p_g}{\partial \rho_g} \right|_{\eta_g}}. \quad (2.59)$$

Though there are only six distinct eigenvalues, it is possible to find seven linearly independent eigenvectors for these eigenvalues. This means that the system of equations is hyperbolic, and is well posed as an initial value problem.

2.4.2 Energy Diffusion

Permitting energy diffusion, that is $k_s \neq 0$ and $k_g \neq 0$, but not momentum diffusion ($\mu_s = \mu_g = 0$), though still not physically meaningful, generates an interesting result.

By including Fourier heat conduction, the dimension of the system rises to $n = 9$. Powers [15], after detailed analysis, reports that the generalized eigenvalues are:

$$\lambda = \begin{cases} u_s \\ u_s \pm \sqrt{\frac{\partial p_s}{\partial \rho_s} \Big|_{T_s, \phi_s} + \frac{\partial p_s}{\partial T_s} \Big|_{\rho_s, \phi_s} \left(\frac{T_s}{\rho_s^2 c_{vs}} \frac{\partial p_s}{\partial T_s} \Big|_{\rho_s, \phi_s} - \frac{\partial T_s}{\partial \rho_s} \Big|_{\eta_s, \phi_s} \right)} \\ u_g \pm \sqrt{\frac{\partial p_g}{\partial \rho_g} \Big|_{T_g} + \frac{\partial p_g}{\partial T_g} \Big|_{\rho_g} \left(\frac{T_g}{\rho_g^2 c_{vg}} \frac{\partial p_g}{\partial T_g} \Big|_{\rho_g} - \frac{\partial T_g}{\partial \rho_g} \Big|_{\eta_g} \right)} \end{cases}. \quad (2.60)$$

These five generalized eigenvalues are all real and distinct. While there are five corresponding generalized eigenvectors, for the generalized eigenvalues, there are not enough generalized eigenvectors to transform the entire system into characteristic form. Therefore the system with energy, but not momentum diffusion, is parabolic. With proper selection of boundary conditions on T_s and T_g , the boundary/initial condition problem is well posed. With five initial conditions, and four boundary conditions (of Dirichlet, Neumann, or mixed form) on solid and gas temperatures, there are enough conditions for the full set of nine equations to be well posed.

2.4.3 Momentum and Energy Diffusion

For the physically important scenario where the system has both momentum and energy diffusion, through Fourier heat transfer and viscous stress, the dimension rises to $n = 11$. Seeking, again, the generalized eigenvalues, and generalized eigenvectors, it is possible to show that there are three real generalized eigenvalues:

$$\lambda = u_s, u_s, u_g. \quad (2.61)$$

Even though not all of the eigenvalues are distinct, there are three generalized eigenvectors. This means that the system cannot be cast into characteristic form, and thereby be hyperbolic; it is, however, parabolic. Therefore, by specifying eight initial conditions (one on each of two boundaries for T_s, T_g, u_s , and u_g) of appropriate Dirichlet, Neumann or mixed form, and three initial conditions on the other

variables, it is reasonable to suppose that there are enough conditions for a well posed system of eleven equations.

2.5 Boundary Conditions

Boundary conditions must be well chosen in order to assure that the problem is solvable. For many of the problems solved in this study, the boundaries were thermally insulated, and satisfied a no-slip condition along geometrical edges. For the one-dimensional case with a domain of length L , that means that,

$$u_s(0, t) = u_s(L, t) = u_g(0, t) = u_g(L, t) = 0, \quad (2.62)$$

$$\frac{\partial T_s}{\partial x}(0, t) = \frac{\partial T_s}{\partial x}(L, t) = \frac{\partial T_g}{\partial x}(0, t) = \frac{\partial T_g}{\partial x}(L, t). \quad (2.63)$$

By extension, for two-dimensional cases with no-slip, thermally insulated boundaries, the conditions are:

$$u_s(y = 0, t) = u_s(y = H, t) = u_g(y = 0, t) = u_g(y = H, t) = 0, \quad (2.64)$$

$$v_s(x = 0, t) = v_s(x = L, t) = v_g(x = 0, t) = v_g(x = L, t) = 0, \quad (2.65)$$

$$\frac{\partial T_s}{\partial x}(x = 0, t) = \frac{\partial T_s}{\partial x}(x = L, t) = \frac{\partial T_g}{\partial x}(x = 0, t) = \frac{\partial T_g}{\partial x}(x = L, t), \quad (2.66)$$

and

$$\frac{\partial T_s}{\partial y}(y = 0, t) = \frac{\partial T_s}{\partial y}(y = H, t) = \frac{\partial T_g}{\partial y}(y = 0, t) = \frac{\partial T_g}{\partial y}(y = H, t). \quad (2.67)$$

Here, v_s and v_g are the vertical components of velocity, and H is the height of the domain.

For the rest of the problems, most boundaries had periodic boundary conditions, which required that the velocity be the same at the top and the bottom of the domain:

$$u_s(y = 0, t) = u_s(y = H, t) \text{ and } u_g(y = 0, t) = u_g(y = H, t). \quad (2.68)$$

CHAPTER 3

NUMERICAL METHOD

3.1 Equation Forms

Before solving the system of equations (Equations (2.1)–(2.7)), they were first cast into the following form:

$$\frac{\partial \mathbf{g}}{\partial t} + \nabla \cdot \mathbf{\Gamma} = \mathbf{f}. \quad (3.1)$$

This is the nearly conservative form of Equations (2.1)–(2.7) with appropriate forcing terms.

The independent variables appear in Equation (3.1) through \mathbf{g} , which is a 9×1 vector made up of the following components:

$$\mathbf{g} \equiv \begin{bmatrix} g_1 \\ g_2 \\ g_3 \\ g_4 \\ g_5 \\ g_6 \\ g_7 \\ g_8 \\ g_9 \end{bmatrix} \equiv \begin{bmatrix} \rho_s \phi_s \\ \rho_s \phi_s u_s \\ \rho_s \phi_s v_s \\ \rho_s \phi_s \left(e_s + \frac{1}{2}(u_s^2 + v_s^2) \right) \\ \rho_s \\ \rho_g \phi_g \\ \rho_g \phi_g u_g \\ \rho_g \phi_g v_g \\ \rho_g \phi_g \left(e_g + \frac{1}{2}(u_g^2 + v_g^2) \right) \end{bmatrix}. \quad (3.2)$$

From these relations, and using Equation (2.24), the physical variables are defined as:

$$\rho_s = g_5, \quad (3.3)$$

$$u_s = g_2/g_1, \quad (3.4)$$

$$v_s = g_3/g_1, \quad (3.5)$$

$$\phi_s = g_1/g_5, \quad (3.6)$$

$$e_s = \frac{g_4}{g_1} - \frac{1}{2} \left(\frac{g_2^2 + g_3^2}{g_1^2} \right), \quad (3.7)$$

$$\rho_g = g_6/(1 - g_1/g_5), \quad (3.8)$$

$$u_g = g_7/g_6, \quad (3.9)$$

$$v_g = g_8/g_6, \quad (3.10)$$

$$\phi_g = 1 - (g_1/g_5), \quad (3.11)$$

$$e_g = \frac{g_9}{g_6} - \frac{1}{2} \left(\frac{g_7^2 + g_8^2}{g_6^2} \right). \quad (3.12)$$

The term $\mathbf{\Gamma}$ is actually a 9×2 matrix containing the terms associated with the divergence operator in Equation (3.1):

$$\mathbf{\Gamma} = \begin{bmatrix} \rho_s \phi_s \mathbf{u}_s \\ (\rho_s \phi_s \mathbf{u}_s \mathbf{u}_s^T + \phi_s (p_s \mathbf{I} - \boldsymbol{\tau}_s)) \\ (\rho_s \phi_s \mathbf{u}_s (e_s + \frac{1}{2} \mathbf{u}_s \mathbf{u}_s^T) + \phi_s \mathbf{u}_s \cdot (p_s \mathbf{I} - \boldsymbol{\tau}_s) + \phi_s \mathbf{q}_s) \\ \rho_s \mathbf{u}_s \\ \rho_g \phi_g \mathbf{u}_g \\ (\rho_g \phi_g \mathbf{u}_g \mathbf{u}_g^T + \phi_g (p_g \mathbf{I} - \boldsymbol{\tau}_g)) \\ (\rho_g \phi_g \mathbf{u}_g (e_g + \frac{1}{2} \mathbf{u}_g \mathbf{u}_g^T) + \phi_g \mathbf{u}_g \cdot (p_g \mathbf{I} - \boldsymbol{\tau}_g) + \phi_g \mathbf{q}_g) \end{bmatrix}. \quad (3.13)$$

The full expansion of Equation (3.13) is given in Equation (3.14) using constitutive relations Equations (2.33)–(2.45).

$$\mathbf{\Gamma} = \begin{bmatrix}
\rho_s \phi_s u_s & \rho_s \phi_s v_s \\
\rho_s \phi_s u_s^2 + p_s \phi_s - \phi_s \tau_{s11} & \rho_s \phi_s u_s v_s - \phi_s \tau_{s12} \\
\rho_s \phi_s u_s v_s - \phi_s \tau_{s21} & \rho_s \phi_s v_s^2 + p_s \phi_s - \phi_s \tau_{s22} \\
(\rho_s \phi_s u_s (e_s + \frac{1}{2}(u_s^2 + v_s^2)) + p_s \phi_s u_s - \phi_s (u_s \tau_{s11} + v_s \tau_{s12}) + \phi_s q_{s1}) & (\rho_s \phi_s v_s (e_s + \frac{1}{2}(u_s^2 + v_s^2)) + p_s \phi_s v_s - \phi_s (u_s \tau_{s21} + v_s \tau_{s22}) + \phi_s q_{s2}) \\
\rho_s u_s & \rho_s v_s \\
\rho_g \phi_g u_g & \rho_g \phi_g v_g \\
\rho_g \phi_g u_g^2 + p_g \phi_g - \phi_g \tau_{g11} & \rho_g \phi_g u_g v_g - \phi_g \tau_{g12} \\
\rho_g \phi_g u_g v_g - \phi_g \tau_{g21} & \rho_g \phi_g v_g^2 + p_g \phi_g - \phi_g \tau_{g22} \\
(\rho_g \phi_g u_g (e_g + \frac{1}{2}(u_g^2 + v_g^2)) + p_g \phi_g u_g - \phi_g (u_g \tau_{g11} + v_g \tau_{g12}) + \phi_g q_{g1}) & (\rho_g \phi_g v_g (e_g + \frac{1}{2}(u_g^2 + v_g^2)) + p_g \phi_g v_g - \phi_g (u_g \tau_{g21} + v_g \tau_{g22}) + \phi_g q_{g2})
\end{bmatrix}. \tag{3.14}$$

The expanded forms of $\boldsymbol{\tau}$ and \mathbf{q} , which appear in $\mathbf{\Gamma}$ are:

$$\boldsymbol{\tau}_s = 2\mu_s \begin{bmatrix}
\frac{\partial u_s}{\partial x} - \frac{1}{3} \left(\frac{\partial u_s}{\partial x} + \frac{\partial v_s}{\partial y} \right) & \frac{1}{2} \left(\frac{\partial u_s}{\partial y} + \frac{\partial v_s}{\partial x} \right) \\
\frac{1}{2} \left(\frac{\partial u_s}{\partial y} + \frac{\partial v_s}{\partial x} \right) & \frac{\partial u_s}{\partial x} - \frac{1}{3} \left(\frac{\partial v_s}{\partial y} + \frac{\partial u_s}{\partial x} \right)
\end{bmatrix}, \tag{3.15}$$

$$\boldsymbol{\tau}_g = 2\mu_g \begin{bmatrix} \frac{\partial u_g}{\partial x} - \frac{1}{3} \left(\frac{\partial u_g}{\partial x} + \frac{\partial v_g}{\partial y} \right) & \frac{1}{2} \left(\frac{\partial u_g}{\partial y} + \frac{\partial v_g}{\partial x} \right) \\ \frac{1}{2} \left(\frac{\partial u_g}{\partial y} + \frac{\partial v_g}{\partial x} \right) & \frac{\partial u_g}{\partial x} - \frac{1}{3} \left(\frac{\partial v_g}{\partial y} + \frac{\partial u_g}{\partial x} \right) \end{bmatrix}, \quad (3.16)$$

$$\mathbf{q}_s = \begin{bmatrix} -k_s \frac{\partial T_s}{\partial x} \\ -k_s \frac{\partial T_s}{\partial y} \end{bmatrix}, \quad (3.17)$$

$$\mathbf{q}_g = \begin{bmatrix} -k_g \frac{\partial T_g}{\partial x} \\ -k_g \frac{\partial T_g}{\partial y} \end{bmatrix}. \quad (3.18)$$

The forcing functions give an \mathbf{f} vector:

$$\mathbf{f} = \begin{bmatrix} \mathcal{C} \\ \mathcal{M}_x \\ \mathcal{M}_y \\ \mathcal{E} + \mathcal{S}_e \\ -\mathcal{F}\rho_s/\phi_s \\ -\mathcal{C} \\ -\mathcal{M}_x \\ -\mathcal{M}_y \\ -\mathcal{E} + \mathcal{S}_e \end{bmatrix}. \quad (3.19)$$

The gradient term in \mathcal{M} does not provide any difficulties formulating the problem. Merely split the gradient form of $p_g \nabla \phi_s$ into $p_g \frac{\partial \phi_s}{\partial x}$ and $p_g \frac{\partial \phi_s}{\partial y}$ and put the resulting expressions in the appropriate terms for \mathcal{M}_x and \mathcal{M}_y as in Equation (3.19). In this case,

$$\mathcal{M}_x = p_g \frac{\partial \phi_s}{\partial x} - \delta(u_s - u_g) + \frac{1}{2}(u_s + u_g)\mathcal{C}, \quad (3.20)$$

and

$$\mathcal{M}_y = p_g \frac{\partial \phi_s}{\partial y} - \delta(v_s - v_g) + \frac{1}{2}(v_s + v_g)\mathcal{C}. \quad (3.21)$$

The expansion of \mathcal{E} is

$$\mathcal{E} = \mathcal{H}(T_g - T_s) - p_g \mathcal{F} + u_s \mathcal{M}_x + v_s \mathcal{M}_y + \left(e_s - \frac{u_s^2 + v_s^2}{2} \right) \mathcal{C}. \quad (3.22)$$

Using Equations (3.20)–(3.22) the full expansion of \mathbf{f} , setting \mathcal{C} to zero, as it was for all of this study, and including \mathcal{S}_e is

$$\mathbf{f} = \begin{bmatrix} 0 \\ p_g \frac{\partial \phi_s}{\partial x} - \delta(u_s - u_g) \\ p_g \frac{\partial \phi_s}{\partial y} - \delta(v_s - v_g) \\ \mathcal{S}_e + \mathcal{H}(T_g - T_s) - p_g (\phi_s \phi_g / \mu_c (p_s - p_g - \beta_s)) + \\ u_s (p_g \frac{\partial \phi_s}{\partial x} - \delta(u_s - u_g)) + v_s (p_g \frac{\partial \phi_s}{\partial y} - \delta(v_s - v_g)) \\ \rho_s \phi_g (p_s - p_g - \beta_s) / \mu_c \\ 0 \\ - (p_g \frac{\partial \phi_s}{\partial x} - \delta(u_s - u_g)) \\ - (p_g \frac{\partial \phi_s}{\partial y} - \delta(v_s - v_g)) \\ \mathcal{S}_e - (\mathcal{H}(T_g - T_s) - p_g (\phi_s \phi_g / \mu_c (p_s - p_g - \beta_s)) + \\ u_s (p_g \frac{\partial \phi_s}{\partial x} - \delta(u_s - u_g)) + v_s (p_g \frac{\partial \phi_s}{\partial y} - \delta(v_s - v_g))) \end{bmatrix}. \quad (3.23)$$

3.2 Numerical Method

FEMLAB [22] is a commercially available partial differential equation (PDE) solver, and was used exclusively for all problems solved in this study. FEMLAB uses the method of lines to solve the problem. The spatial domain is first discretized into a large number of finite elements, reducing the system to a large system of ordinary

differential equations (ODE's). The time advancement algorithm is a version of the differential/algebraic equation (DAE) solver called DASPK. This solver uses variable-order, variable-step-size backward differentiation formulas to generate a linear system at each time step.

The resulting linear system is of the form $\mathbf{A} \cdot \mathbf{x} = \mathbf{b}$. The solver used in all problems in this study is called UMFPACK, which is the most robust linear solver that FEMLAB uses. In these problems, \mathbf{A} is a sparse, non-diagonal square matrix. UMFPACK is a direct solver employing an LU factorization of the matrix \mathbf{A} . Although FEMLAB does have the capability to use adaptive meshes, all meshes used in this study were fixed.

3.3 Meshes and Grid Resolution

FEMLAB selects its own mesh sizes based on the geometry of the domain, and various internal parameters. The operator of the code is free to refine any or all of the domain to use a finer mesh. The mesh FEMLAB generates is not uniform, so in order to determine approximate spacing, and size of mesh points, the following relation was employed to determine the characteristic numerical length, L_c ,

$$L_c \sim \sqrt{\frac{A_{tot}}{N}}. \quad (3.24)$$

Here, A_{tot} is the total domain of the area, and N is the number of elements in the calculation. This approximation is based on the following assumptions:

1. Elements are uniformly distributed across the domain.
2. All elements are shaped as equilateral triangles.
3. The characteristic length is the length of one side of the average sized element.

It is apparent in Chapter 4 that the characteristic length of the elements is sufficiently small to capture the physical scales of the problem.

CHAPTER 4

VERIFICATION

4.1 One-Dimensional Shock Tube

The classical shock tube problem has two domains in which the material is initially at rest and at a uniform temperature. The domains are, however at different pressures and densities. Upon initiation the system is set in motion. A shock then propagates into the lower density region, and a material discontinuity, as well as a rarefaction zone travel into the higher density region. For a calorically perfect, ideal, inviscid gas, an analytic solution exists, as found in Shapiro [23].

All models in these studies included diffusion effects, both of energy and of momentum, within each phase. For the purposes of this verification problem, the coefficients for both gases were selected such that the Prandtl number, $Pr = \gamma\mu c_v/k$, is roughly unity in order to assure that energy and momentum diffused at nearly the same rate.

Figure 4.1 shows the temperature profile at $60 \mu s$ for a shock tube with two ideal, calorically perfect gases. Interphase transport is neglected, but physical diffusion of energy and momentum remain. In order to visualize both waves in the same graph by keeping the waves near one another, γ_g is artificially inflated to a value of $\gamma_g = 2.70$. As seen in Figure 4.1 the predicted results match remarkably well with the analytic solution. The only major difference is that the predicted results have finite wave thicknesses in the shock and rarefaction zones. This is due to the

physical diffusion, which is of sufficient magnitude to make numerical noise effects, such as Gibbs phenomena, and dispersion, unnoticeable.

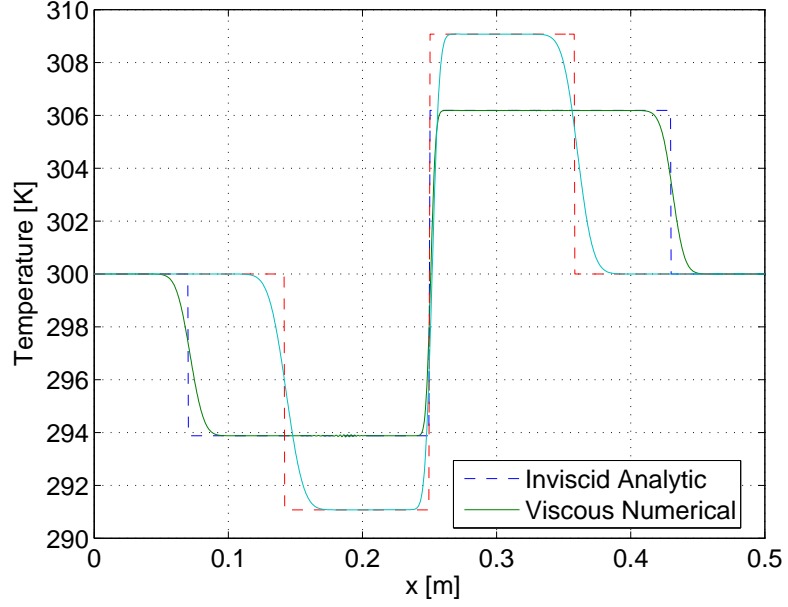


Figure 4.1. Temperature profiles for shock tube at $t = 60 \mu s$

4.2 Convergence and Resolution

4.2.1 Error Norm

As an estimate of the convergence rates of the solver, an approximation of the local error, given as:

$$e_l = \frac{|\rho_{s \max}^e - \rho_{s \max}|}{\rho_{s \max}^e} \quad (4.1)$$

is used. Here, $\rho_{s \max}$ is the maximum value of the solid density for the solution to the equation set for a given mesh and $\rho_{s \max}^e$ is the maximum value of the solid density for the solution to a highly resolved mesh, numbering 32,768 nodes. For the

purposes of these calculations, this is taken to be the exact solution to the problem. It is clear from Figure 4.2 that the error of Equation (4.1) is converging to zero at a uniform rate of about $\mathcal{O}(\Delta x^{2.7})$, which is a faster convergence than the expected second order. It was necessary to do a simple point convergence test on these meshes, since the exact location of the node points shifted with each change in the mesh. It was therefore difficult to find a way to compare all points across the entire geometry to develop a domain convergence test, which is a better approximation of the error, and would give a better estimate of the convergence of the system.

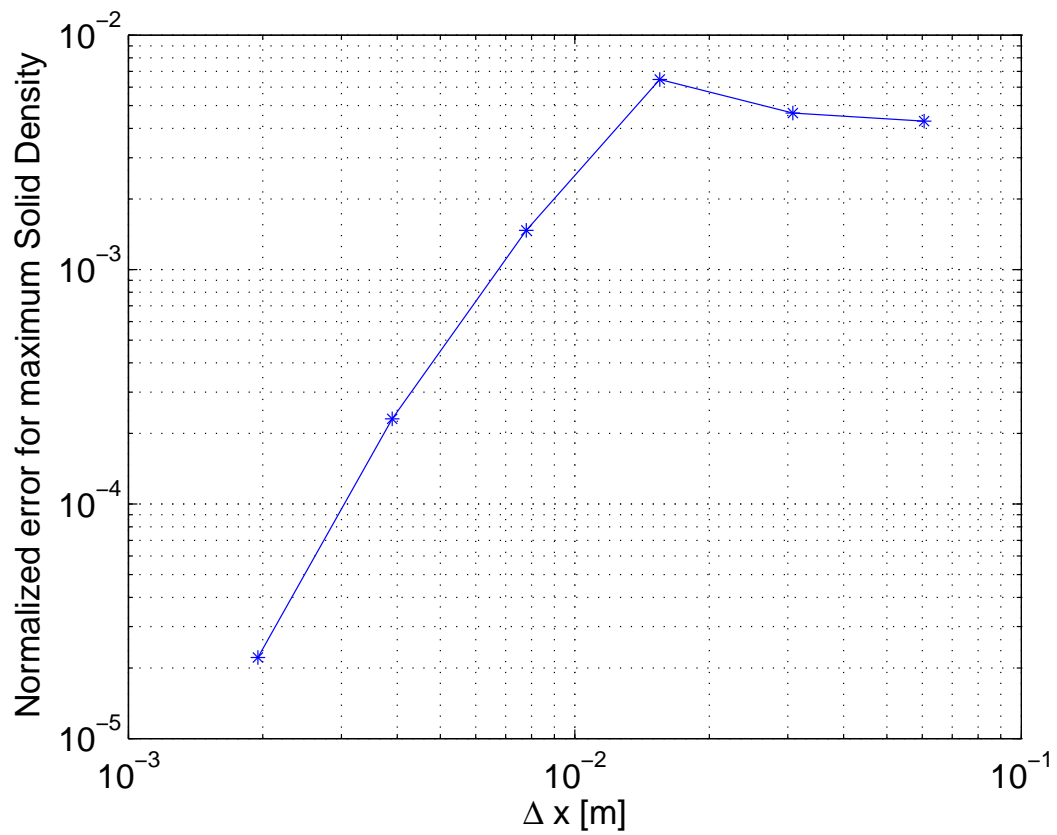


Figure 4.2. Numerical convergence of solid density

4.2.2 Shock Thickness

By assuming that all of the terms in Equation (2.4) are roughly equal in magnitude, it is possible to approximate the shock thickness of the wave. Take, for example, in the one-dimensional steady limit:

$$\phi_g \rho_g u_g^2 \sim \tau_g = \phi_g \frac{4}{3} \mu_g \frac{du_g}{dx}. \quad (4.2)$$

The following approximation for the derivative:

$$\frac{du_g}{dx} \approx \frac{u_{g2} - u_{g1}}{\Theta}, \quad (4.3)$$

where u_{g1} and u_{g2} are pre- and post-shock velocities respectively, when substituted into Equation (4.2), after some rearrangement, gives the following estimate for the shock thickness, Θ :

$$\Theta \sim \frac{\mu_g}{\rho_g} \frac{u_{g2} - u_{g1}}{u_{g2}^2}. \quad (4.4)$$

The shock thickness for the gas, then, is approximately 1 *cm* in length. As seen in Figure 4.2, the meshes used were clearly in the convergent range, and somewhat less than the minimum length scale, indicating that the shock structures are resolved.

4.3 Piston-Driven Problems

The other major class of problems examined, which has benchmark solutions, is that of piston-driven shocks. In this scenario, the bed of material has one boundary into which a piston drives. This squeezes the material and establishes a wave that travels ahead of the piston face. The piston motion is modeled in the following way:

$$u_p(t) = u_p^{max} \left[1 - \exp\left(-\frac{t}{t_{rise}}\right) \right]. \quad (4.5)$$

The rise time of the piston is represented by t_{rise} and the maximum piston velocity is u_p^{max} .

To accomplish this, mathematically, the governing equations (Equation (2.1)–Equation (2.7)) were transformed as:

$$\hat{x} = x - u_p^{max} \left(t + t_{rise} \left[\exp \left(\frac{t}{t_{rise}} \right) - 1 \right] \right). \quad (4.6)$$

Performing the transformation gives the new velocities as:

$$\hat{u}_s = u_s - u_p^{max} \left[1 - \exp \left(\frac{t}{t_{rise}} \right) \right], \quad (4.7)$$

$$\hat{u}_g = u_g - u_p^{max} \left[1 - \exp \left(\frac{t}{t_{rise}} \right) \right]. \quad (4.8)$$

The resultant accelerations are, then:

$$\frac{d\hat{u}_s}{dt_s} = \frac{du_s}{dt_s} - \frac{u_p^{max}}{t_{rise}} \left[\exp \left(-\frac{t}{t_{rise}} \right) \right], \quad (4.9)$$

$$\frac{d\hat{u}_g}{dt_g} = \frac{du_g}{dt_g} - \frac{u_p^{max}}{t_{rise}} \left[\exp \left(-\frac{t}{t_{rise}} \right) \right]. \quad (4.10)$$

In effect, this means that the reference frame is attached to the accelerating piston face, and the domain experiences a non-Galilean transformation. The tube is sufficiently long that there were no effects at the right end of the domain. The result is that there is an effective body force introduced into the right side of Equation (2.3) and Equation (2.4). After solving, the inverse transformation is used to bring the results into the laboratory frame.

4.4 Compaction Wave

Solving the piston problem with no heat transfer nor drag, yields the results shown in Figure 4.3, which shows the solid volume fraction (ϕ_s). The velocity of the piston is 100 m/s , and there is a compaction wave traveling ahead of the piston face at a speed of approximately 380 m/s . Experimental data, and previous numerical work, show this phenomenon. Generally, these works show a compaction wave traveling at 400 m/s ahead of the 100 m/s piston. The characteristic numerical length (Equation (3.24)) is $5.77 \times 10^{-3} m$, which is within the convergent range, and fine enough to capture the smallest physical length scales of the problem (Equation (4.4)) which is approximately 1 cm .

The predicted compaction wave speed is somewhat greater than that seen in the literature [1]. This is likely due to the difficulty of estimating the precise location of the wave front, given the finite thickness of the wave. The prediction, however, is within roughly 10% of the reported value.

Figure 4.4 shows the evolution of the wave front, both in time and in space. This plot shows the displacement of the wavefront. As shown, the system has relaxed to a steady state, since the wave is propagating at a uniform speed, as indicated by the strong linear fit to the data in Figure 4.4.

Of further interest, Figure 4.5 shows the variation of the compaction wave speed, U_c with the piston speed U_p for a range of piston speeds. The experimental data from Sandusky [1] is also shown. For many of the piston speeds, the code shows slightly higher compaction wave speeds, although the scatter of the data indicates that the numerical results are still in good agreement with the experimental results.

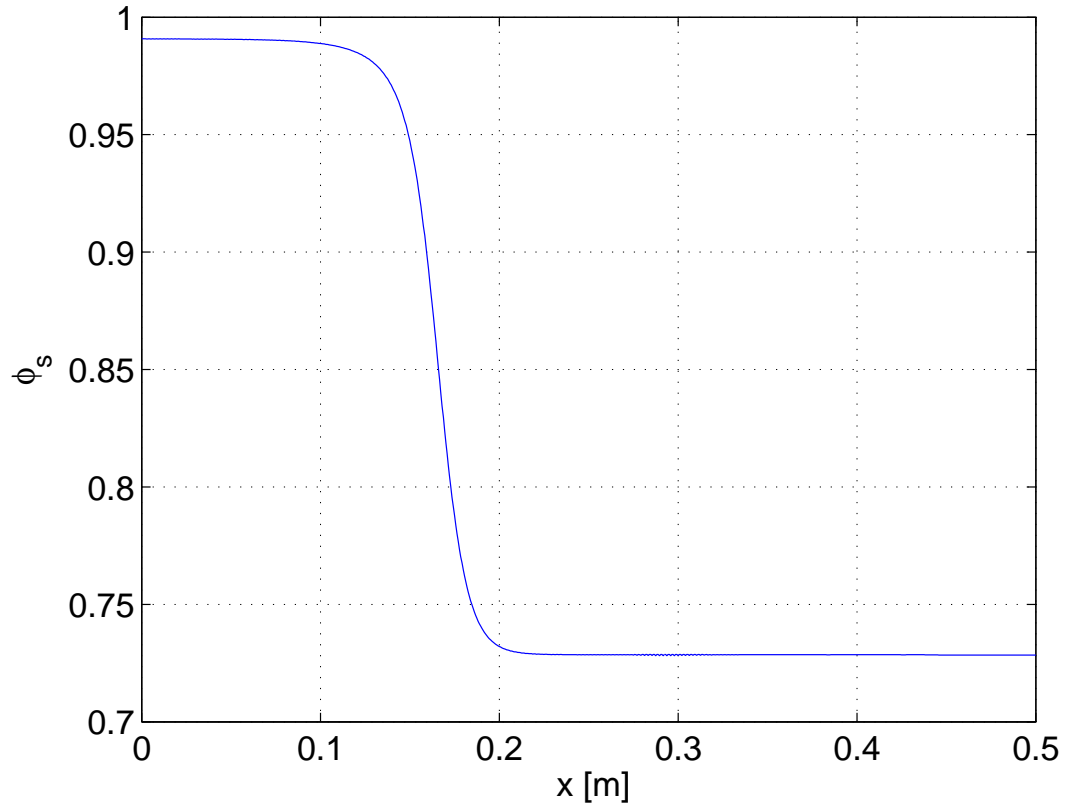


Figure 4.3. Solid volume fraction for a piston at $t = 60 \mu s$

4.5 Stability

A simple demonstration of the stability of the system and the solver was performed, and is discussed here. A stable problem will return to equilibrium after a slight perturbation. To test the stability, a concentrated energy source, of magnitude $10^4 W/m^3$, was imposed on a piston problem, in a region through which the wave had already passed. This source was applied for $3 \mu s$. By examining the time derivative of the gas temperature at the source location, it was obvious that the temperature was relaxing back to the post wave values. Figure 5.1 shows the time derivative of the temperature. This plot shows the first derivative is nega-

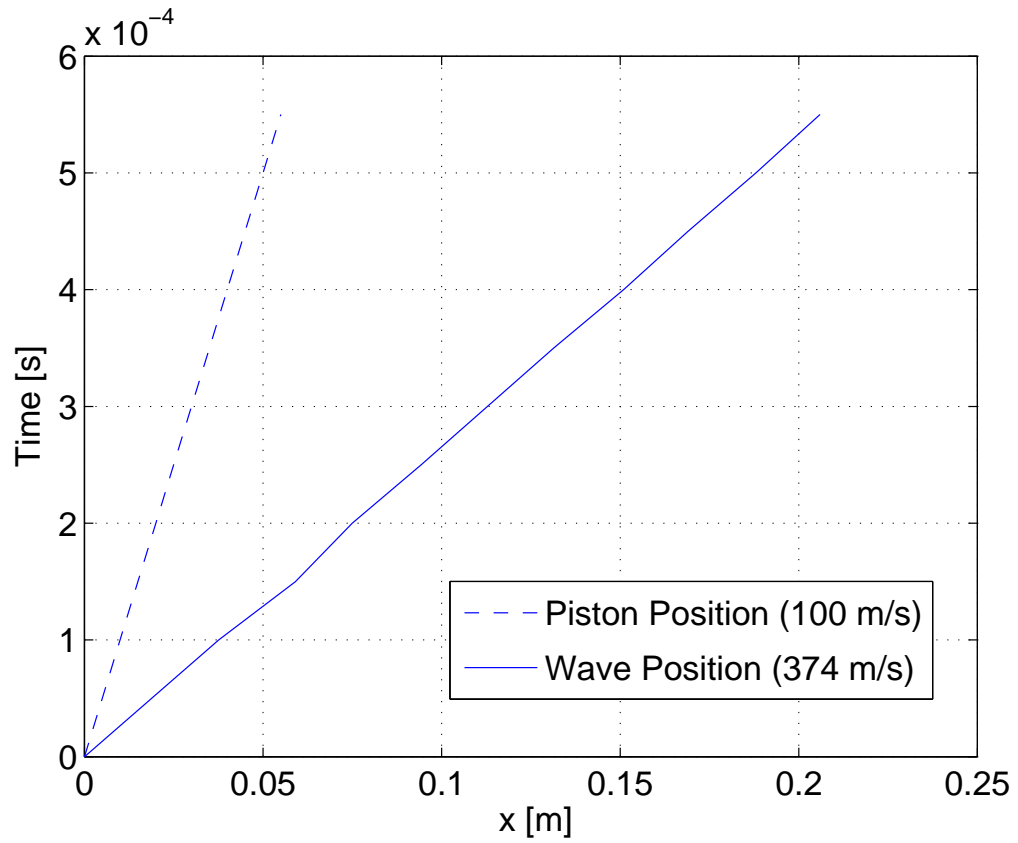


Figure 4.4. $x - t$ plot of the wave front for a piston-driven shock

tive, and that the second derivative is decreasing. These two facts, negative first derivative and decreasing second derivative, are hallmarks of a system relaxing to an equilibrium value.

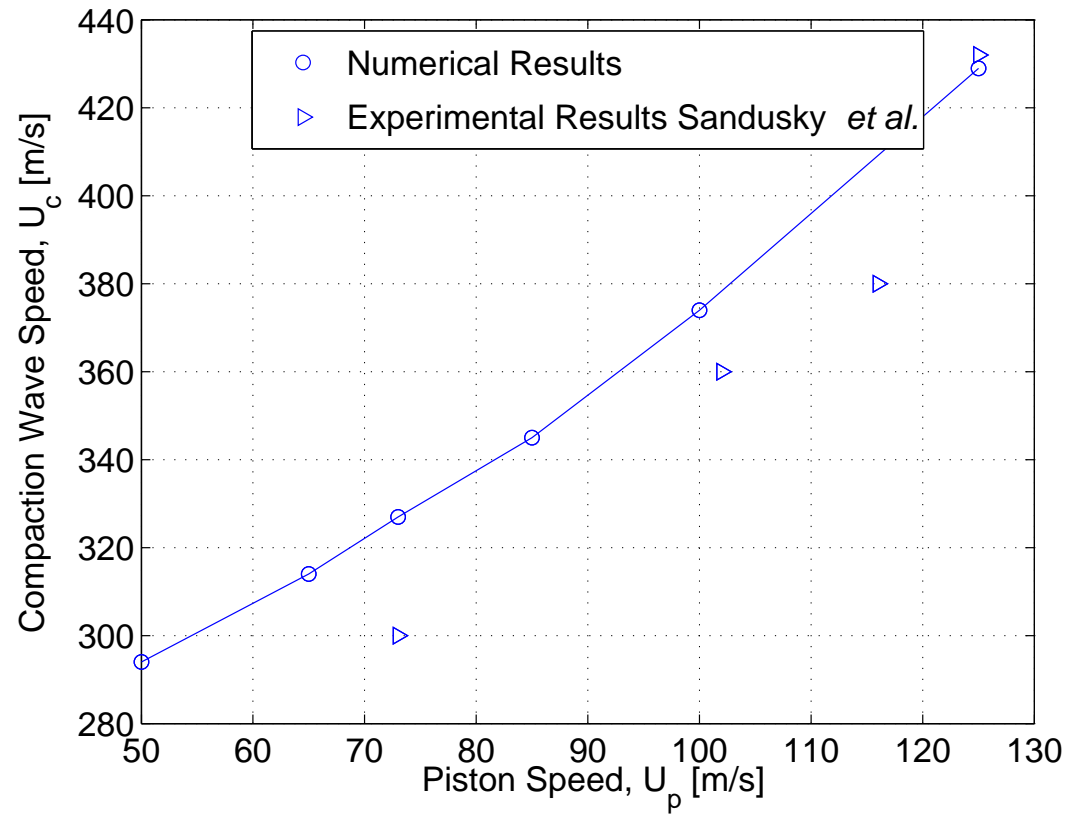


Figure 4.5. Compaction wave speed versus piston speed showing both numerical and experimental results

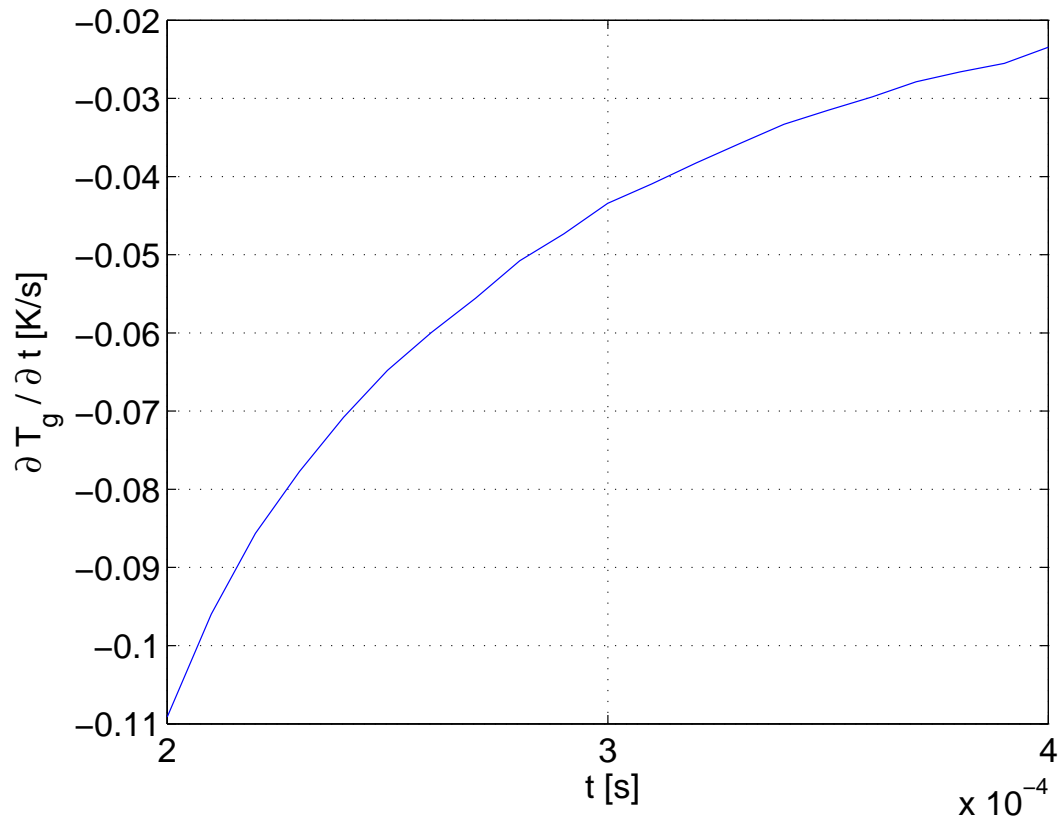


Figure 4.6. Time derivative of gas temperature

CHAPTER 5

RESULTS

5.1 Two-Dimensional Shock Tube

The simplest two-dimensional extension is to use a long narrow tube, with periodic boundary condition along the long edges. The consequent results are essentially a one-dimensional shock tube. These results are for ideal, non-interacting gases in a thermally insulated tube with impermeable walls. (i.e. the exact same conditions as used in the one-dimensional case of Section 4.1.)

Figure 5.1 shows a contour plot of the solid temperature for the shock tube. Figure 5.2 shows a cross section view of the solid and gas temperatures. Note the similarities in Figure 5.2 and Figure 4.1. The characteristic numerical length, from Equation (3.24), for these two-dimensional results is approximately 4 *mm*. Again, the minimum physical length scale is around 1 *cm*, as calculated in Equation (4.4). The solid temperature results from the fully two-dimensional problem with periodic boundary conditions, and the one-dimensional shock tube are indistinguishable even though the results are from a fully two-dimensional code. There is no mechanism driving the y components of velocity or momentum, hence the similarity to the one-dimensional code.

The next logical step is to impose a no-slip boundary condition on all sides of the domain. The results of the solid temperature from such a shock tube are shown in Figure 5.3. Compare Figure 5.1 and Figure 5.3. There are subtle but important

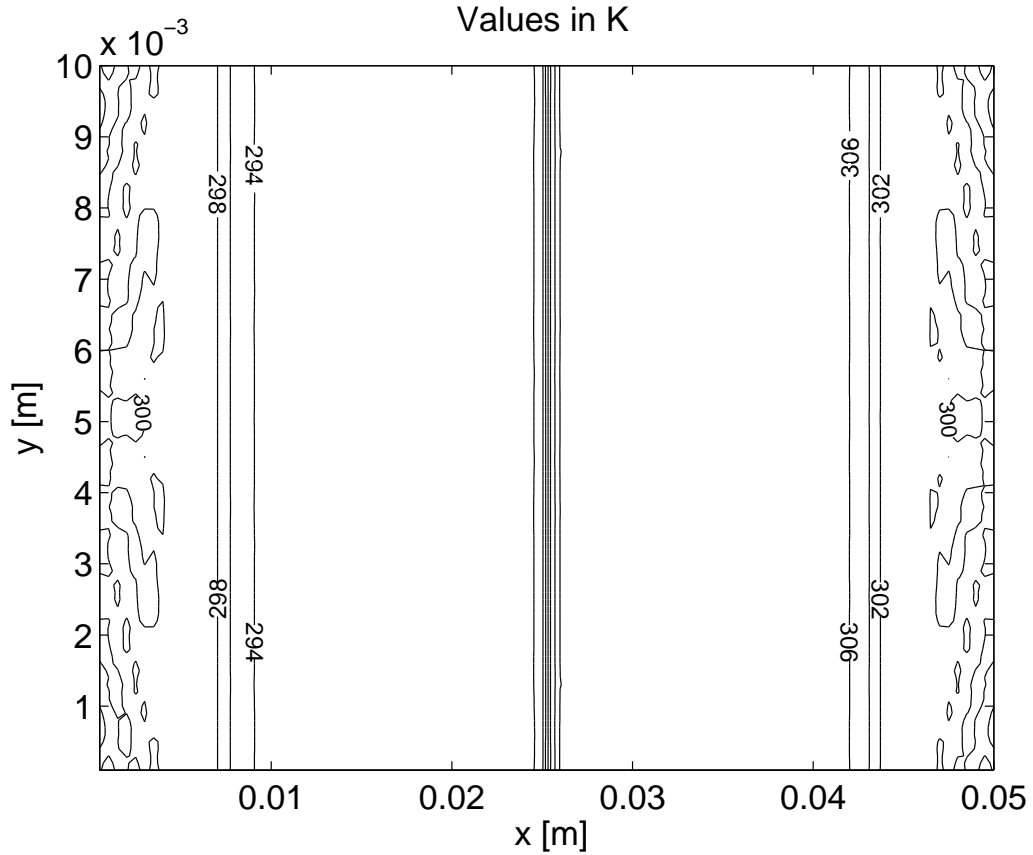


Figure 5.1. Solid temperature for two-dimensional shock tube with periodic boundary conditions at $t = 60 \mu s$

differences. First, there is noticeable curvature in the y direction, in the temperature profile caused by the no-slip condition. As well, the post shock temperature does not stay constant in the x direction as it does for the case with periodic boundary conditions.

A cross section of the domain, (Figure 5.4), through the center of the shock tube ($y = 0.005 m, 0 m < x < .05 m$), shows the profile for gas temperature at $60 \mu s$ for both the periodic and the no slip conditions. The profile of the temperature for the periodic boundary condition shows the classic profile for a one-dimensional shock

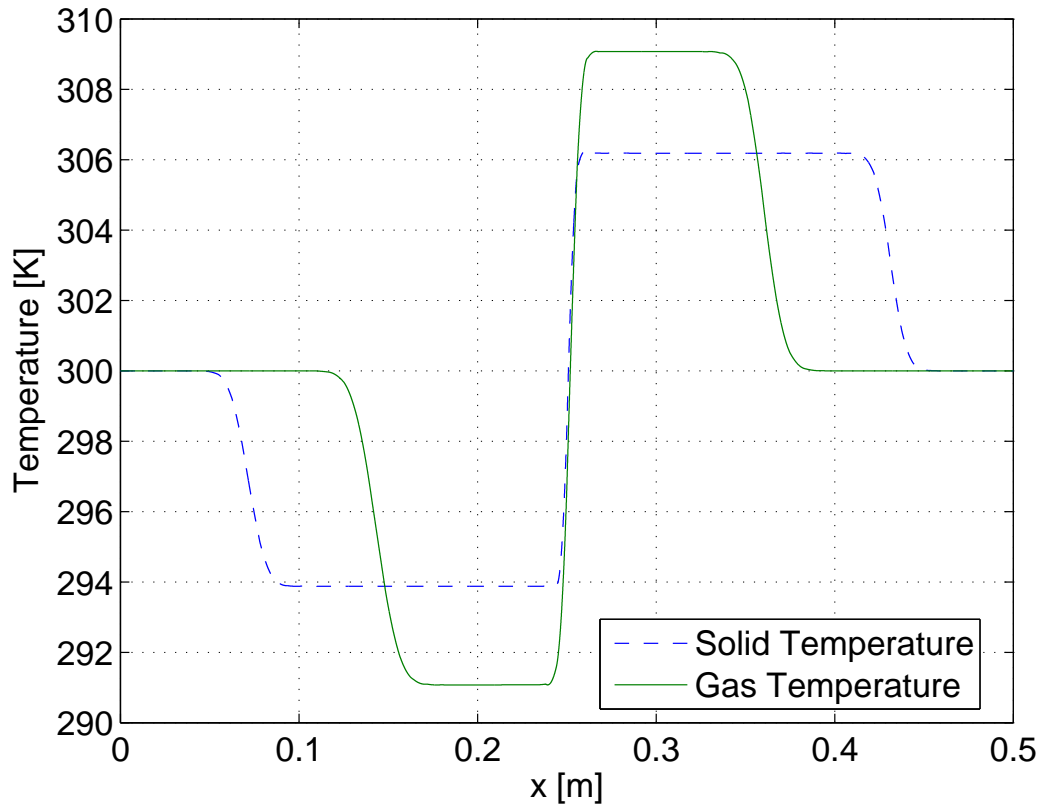


Figure 5.2. Temperature profiles at the centerline for two-dimensional shock tube at $t = 60 \mu s$

tube, such as sharp wave fronts, and constant temperatures in the domains through which the waves have passed. When the no slip boundary condition is imposed, the leading edge of the shock becomes slightly more diffuse, and the temperatures in the domain through which the waves have passed are not constant.

When drag and heat transfer are included in the system, the effects are almost negligible on the solid phase. Due to the much greater density of the solid phase, the gas equilibrates to the solid phase with very little effect to the solid. Figure 5.5 shows the relative difference in the solid temperature profiles defined as:

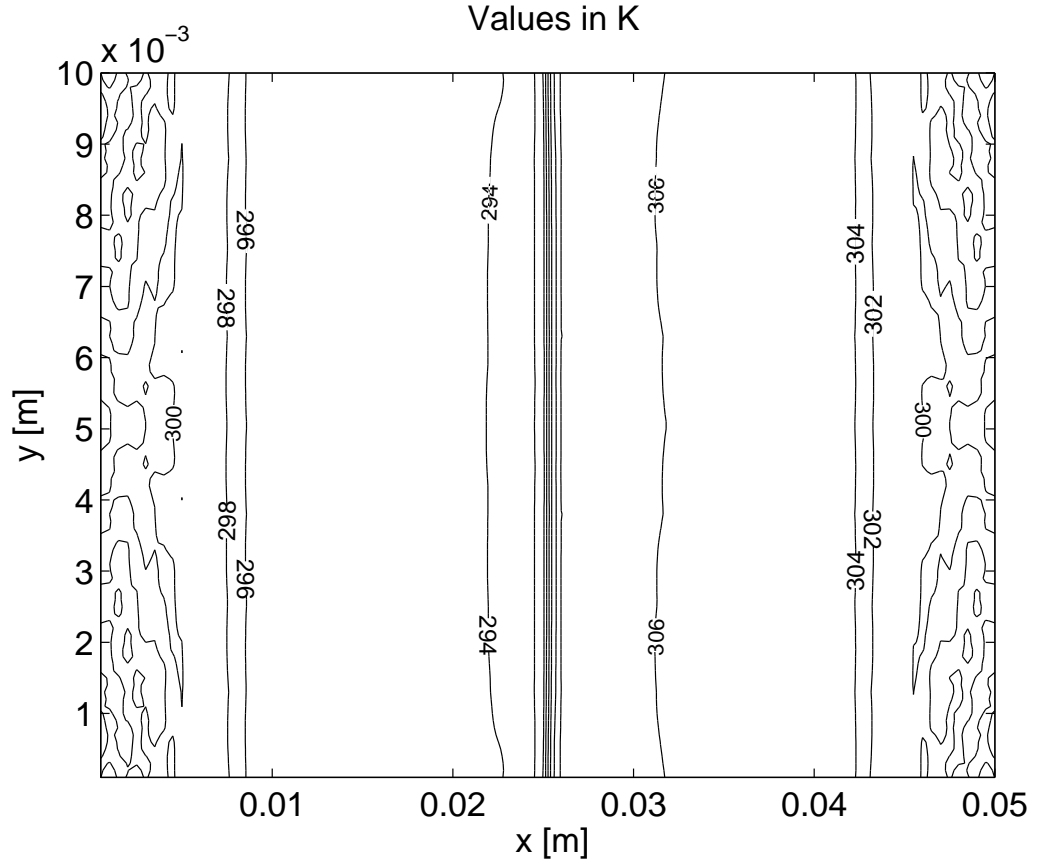


Figure 5.3. Solid temperature for two-dimensional shock tube with no-slip boundary conditions at $t = 60 \mu s$

$$T_d = \frac{T_s - T_{sd}}{T_o}. \quad (5.1)$$

Here, T_s is the solid temperature for the simple shock tube. T_{sd} is the temperature for the same shock tube when diffusion is included, T_d is the relative difference of the two, and T_o is the initial temperature.

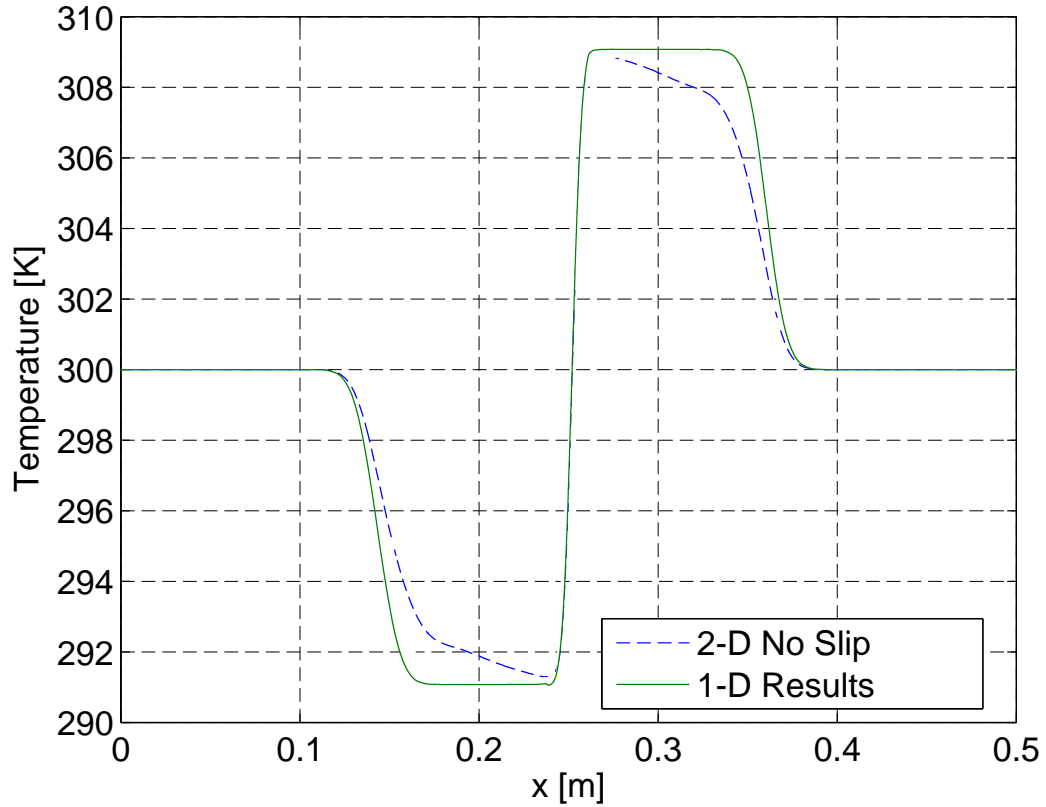


Figure 5.4. Comparison of gas temperature profiles through the center of the domain for no slip and periodic boundary conditions at $t = 60 \mu s$

5.2 Two-Dimensional Piston

For the two-dimensional piston, periodic boundary conditions were introduced at $y = 0 \text{ m}$, $0 \text{ m} < x < 0.5 \text{ m}$ and $y = 0.05 \text{ m}$, $0 \text{ m} < x < 0.5 \text{ m}$, but no further modifications occurred in the forcing functions of the phases (Equations (4.9)–(4.10)), since there was no acceleration in the vertical direction.

As done in Section 5.1 for the simple shock tube, here is a similar comparison of gas temperatures for the piston-driven problem, both for a piston with periodic boundary conditions (Figure 5.6), and for the problem with no-slip boundary con-

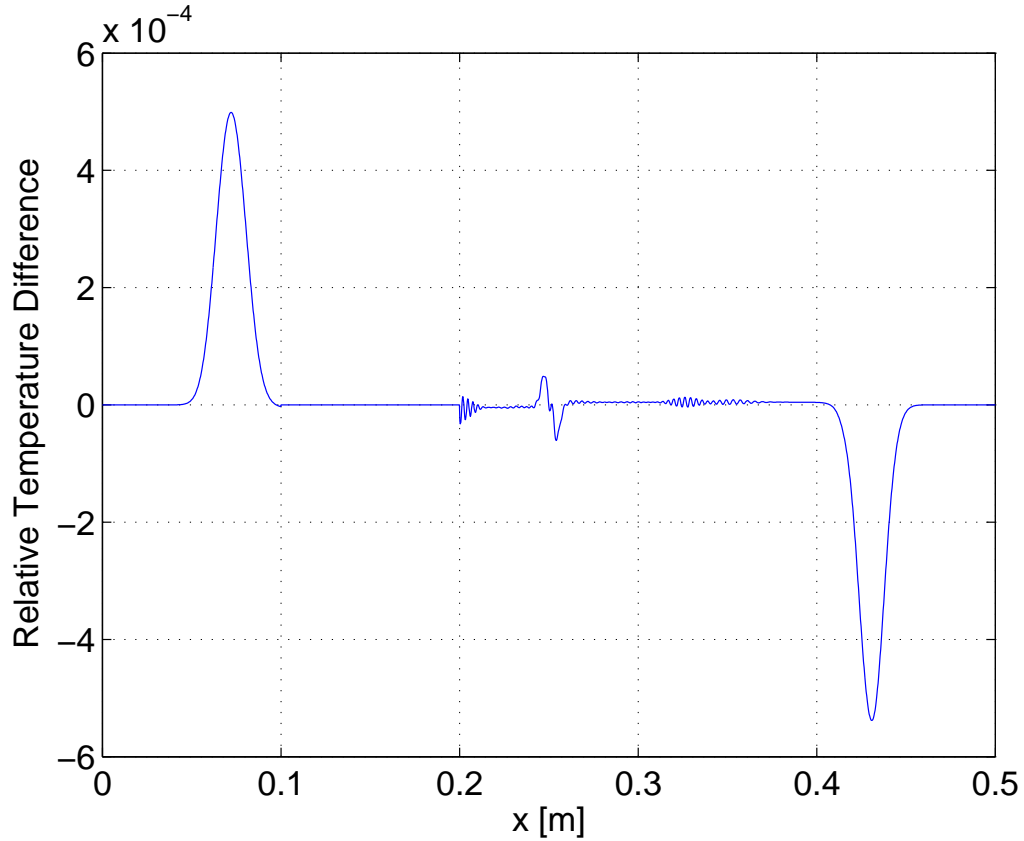


Figure 5.5. Relative difference in solid temperature with and without diffusion of energy and momenta $t = 60 \mu s$

ditions (Figure 5.7). This latter case is not as physically meaningful since there is necessarily slip along the cylinder at the physical piston face, but this exercise gives meaningful insight into the two-dimensional piston problem.

As with the case of the shock tube problem, there are similarities between the speeds of the wave fronts, but there are obvious boundary layer effects in the case with no-slip conditions. This seems to indicate that there are no significant underlying problems with the two-dimensional extension of the equation set.

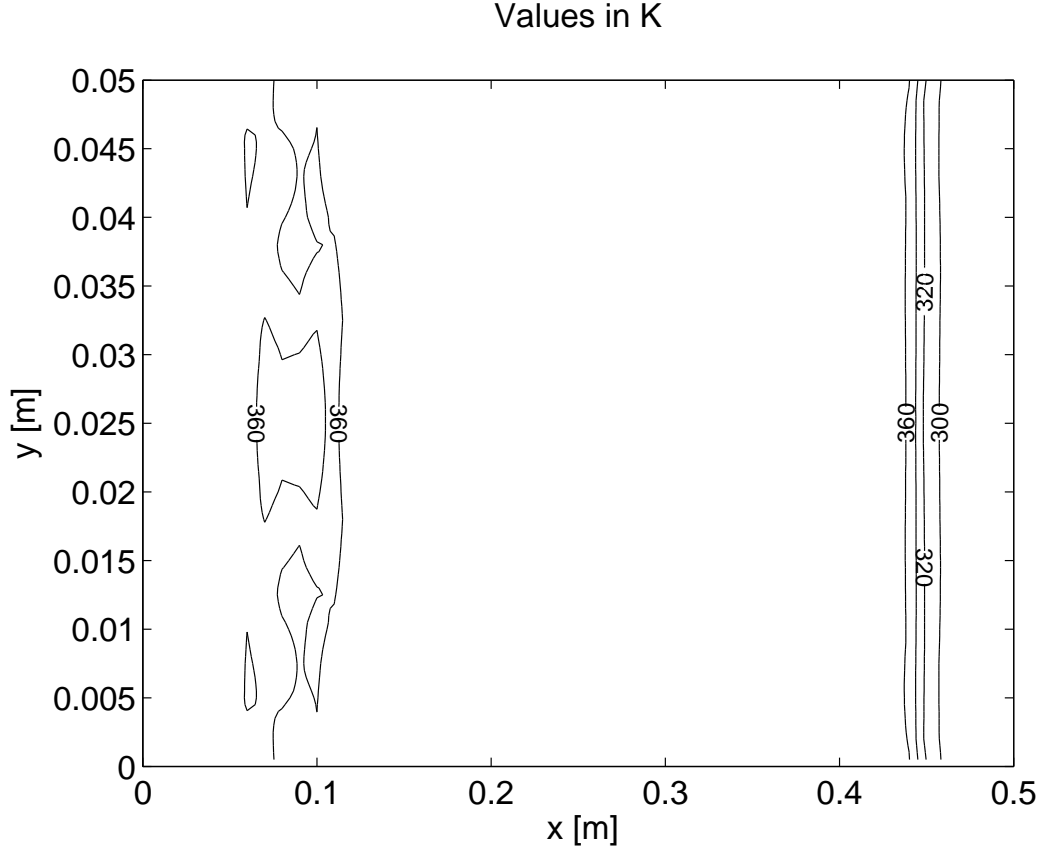


Figure 5.6. Gas temperature for the piston-driven problem with periodic boundary conditions at $t = 600 \mu s$

5.3 Forcing Function

In order to generate meaningful results for the system, a specific choice was made for \mathcal{S}_e ,

$$\mathcal{S}_e = a_o e^{-b_o((x-x_o)^2+(y-y_o)^2)}. \quad (5.2)$$

Equation (5.2) is a narrow two-dimensional Gaussian curve. The amplitude factor a_o has units of W/m^3 , which is energy per unit volume. The steepness of the curve is affected by b_o , which has units of m^{-2} , and x_o and y_o have units of m

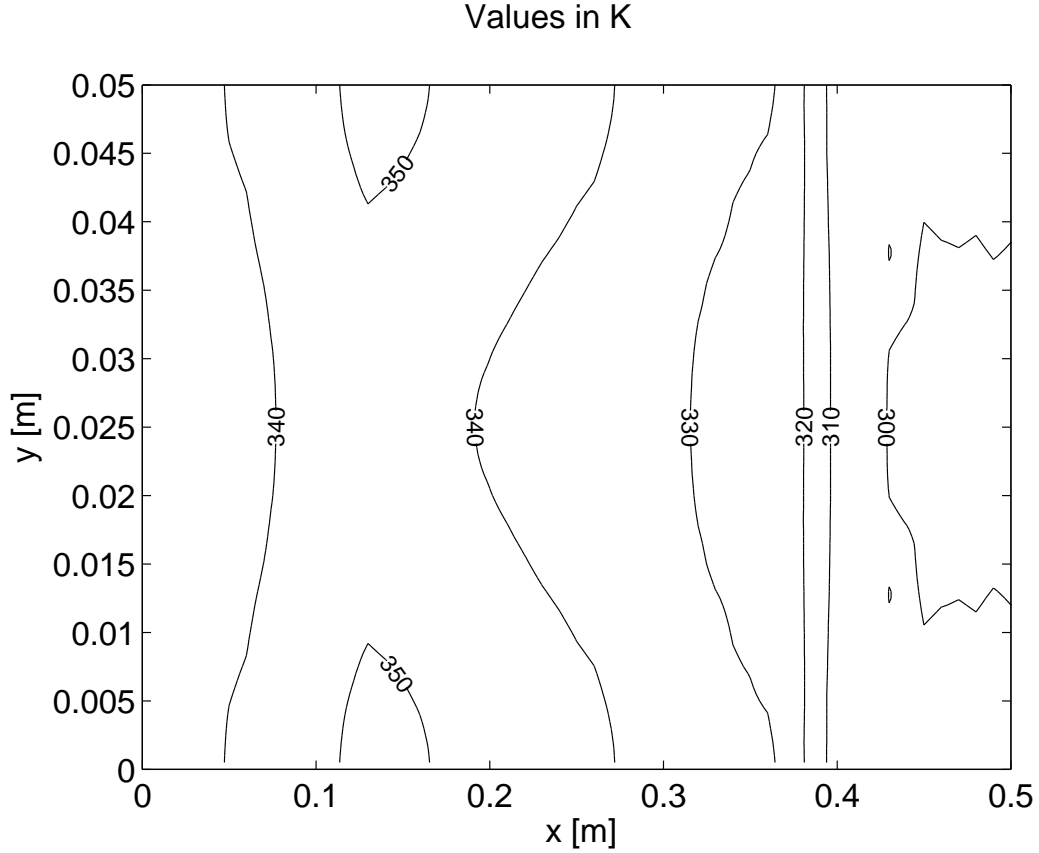


Figure 5.7. Gas temperature for the piston-driven problem with no-slip boundary conditions at $t = 600 \mu s$

and determine the placement of the center of the energy source. Figure 5.8 shows a cross section of the forcing function. It is radially symmetrical and centered at the center of the physical domain.

For some of the simulations, where the length of the domain was much larger than the height, altered form of Equation (5.2) was used. These alteration provides a planar forcing function as follows:

$$\mathcal{S}_e = a_o e^{-b_o((x-x_o)^2)}. \quad (5.3)$$

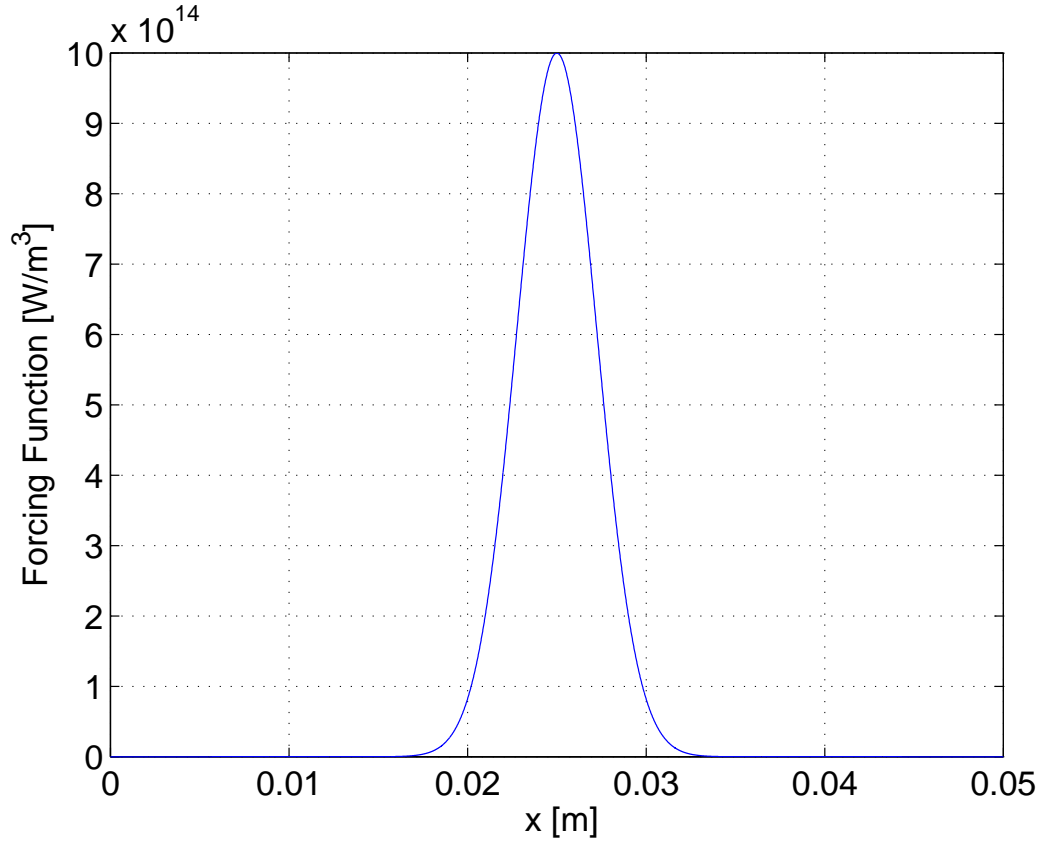


Figure 5.8. Initial profile of source term \mathcal{S}

Since the physical domains for these simulations are on the order of centimeters, it is necessary to choose b_o , in Equation (5.2) sufficiently large to give a concentrated source. In this case, $b_o \sim 10^6 \text{ m}^{-2}$. Furthermore, in order to assure compaction, it was found, after testing several values, that it was necessary to choose $a_o \sim 10^{14} \text{ W/m}^3$. This leads to solid volume fractions close to unity.

5.4 Simple Geometry

The simplest problem is to subject two calorically perfect ideal gases to the source term that appears in the energy equations. Obviously, there will no longer

be conservation of energy, but mass is still conserved. It is worth noting that the heat source causes an initial, and marked decrease in density of the two phases.

In order to demonstrate the physics of the problem, the source function is first applied to a circular region far from any edges to ascertain the behavior of the system independent of geometric considerations. Figure 5.9 and Figure 5.10 show the density cross sections for two calorically perfect ideal, non-interacting gases. These cross sections include the center of the physical domain, and send out disturbances in a radially symmetrical way. There is uniform radial pulse traveling outward for the two gases at the rates of 5000 m/s and 3333 m/s . The sound speeds (c) for these two ideal gases were calculated as:

$$c = \sqrt{\gamma \mathcal{R}T} = \sqrt{\gamma c_v T(\gamma - 1)}. \quad (5.4)$$

For the ideal gas, with the smaller ratio of specific heats, the temperature difference between the pre- and post- wave values was in the range of $\sim 10^3 K$, so the acoustic speed calculated from Equation (5.4) was difficult to approximate. As well, it was not clear where the wave front was, due to its finite thickness. Nonetheless, the predicted wave speed for the other gas was in good agreement with the calculated value. The wave speed observed was approximately 3333 m/s , while the calculation predicted a wave speed of approximately 3000 m/s .

5.5 Long Slender Region

The first geometry studied is a long slender region, subjected to the energy source on one end, with periodic boundary conditions along the long sides of the region. In this way, a wave results, and travels down the tube. Figure 5.12 shows two ideal calorically perfect gases subjected to the energy source. They attain wave speeds of approximately 6300 and 3000 m/s . When the no-slip condition is imposed, there

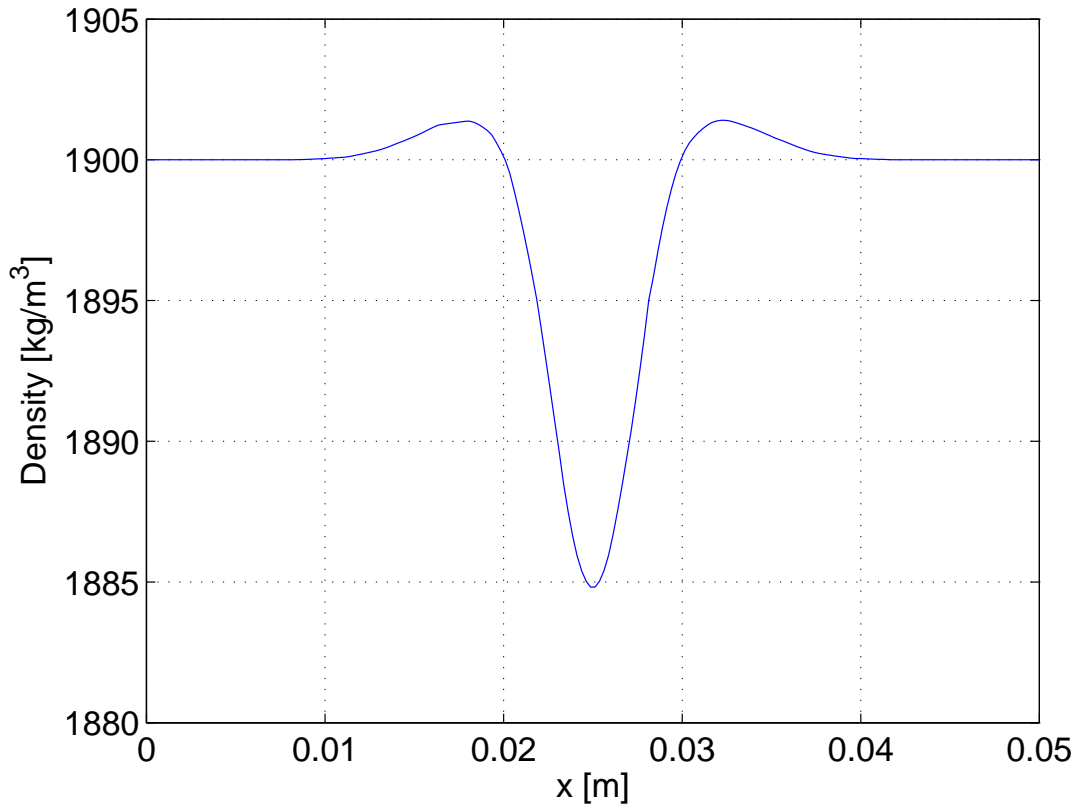


Figure 5.9. Ideal gas density for a concentrated energy source: higher ratio of specific heats at $t = 60 \mu s$

is no significant effect on the wave speeds measured at the center of the channel, though there is a marked overall effect, as shown in comparison of the contour plots of gas density in Figure 5.11 and Figure 5.12. (The representation of the physical domain has been altered to allow for better visualization of the data. In particular, the aspect ratio of height to width has been made approximately one.) The differences in these two are mainly in the form of boundary layer effects on the trailing low density region in the tube.

A cross section plot of the gas density (Figure 5.13), across the long axis of the

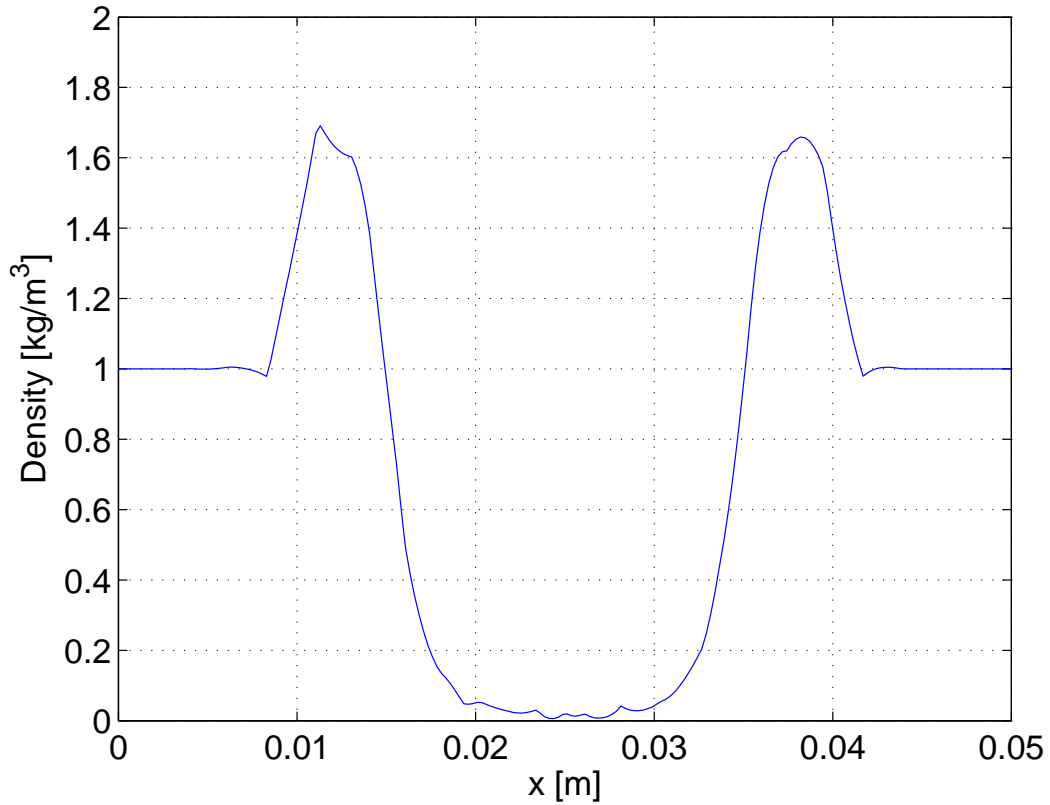


Figure 5.10. Ideal gas density for a concentrated energy source: lower ratio of specific heats at $t = 60 \mu s$

region, is provided to give a better sense of the densities encountered in this study.

5.6 Annulus

For a more geometrically interesting problem an annulus was chosen. Figure 5.14 shows a contour plot of the initial forcing function. In this case, the annulus is subjected to a concentrated energy source, which induces compaction.

These results are for the problem where drag, compaction, and heat transfer are all present. Notice, again, the significant decrease in density of phases at the site of the energy source in Figure 5.15.

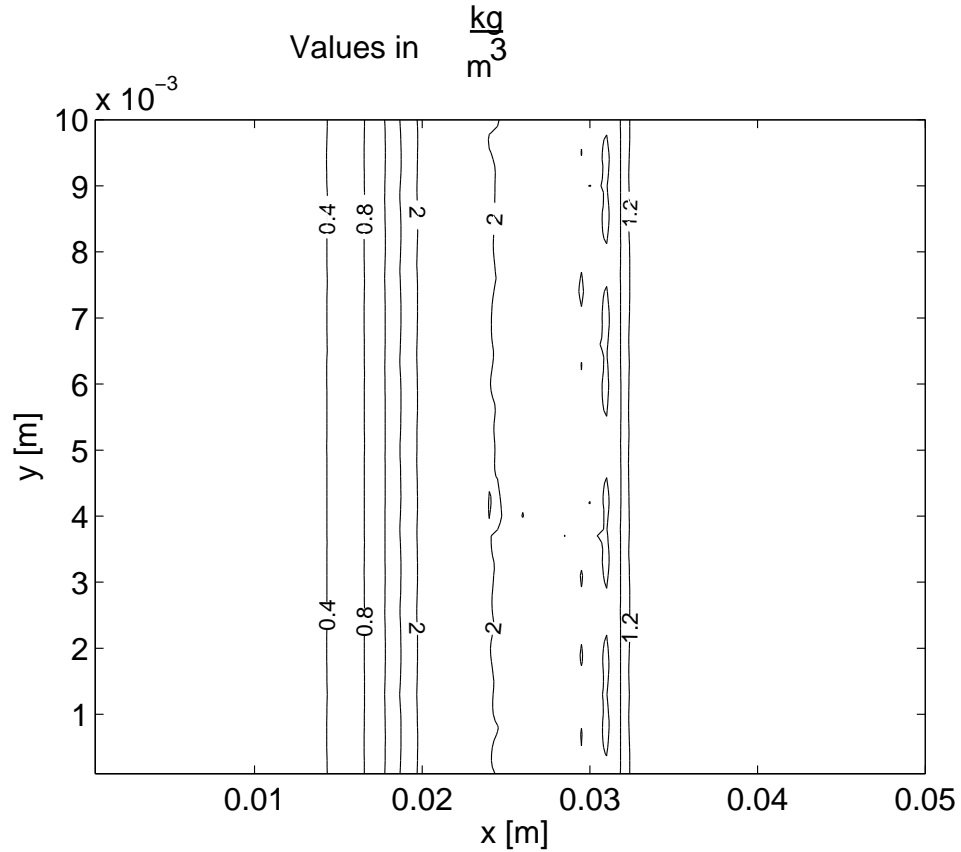


Figure 5.11. Gas density for a concentrated energy source with periodic boundary conditions at $t = 50 \mu s$

Notice in Figure 5.16 that the energy source has caused the volume fraction of the solid (ϕ_s) to approach unity.

Physically, this means that the solid-gas matrix has squeezed in on itself leaving a nearly solid region with small pockets of denser gas. As well, the compaction zone has traveled uniformly outward from the initiation point. At the geometric edges of the region, the no-slip boundary condition has caused these waves to attach to the walls. This is most evident in Figure 5.17 which shows the kinetic energy per unit volume of the system, where kinetic energy, E_k is given by:

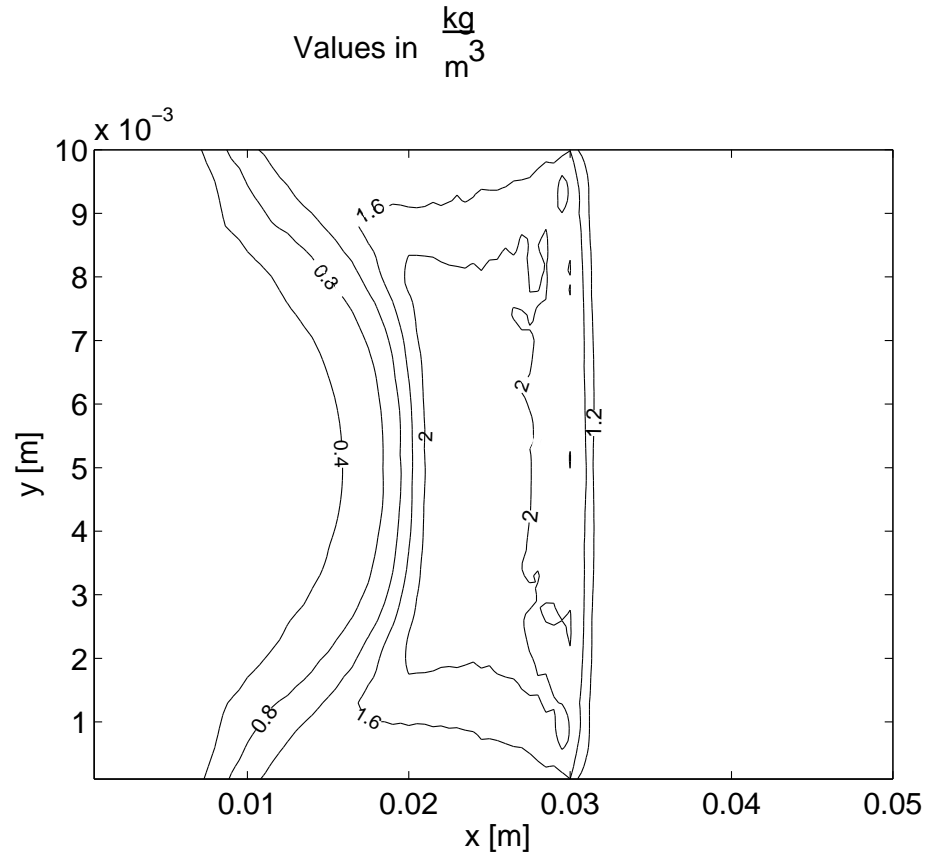


Figure 5.12. Gas density for a concentrated energy source with periodic boundary conditions at $t = 50 \mu s$

$$E_k = \frac{1}{2} \rho_s \phi_s (u_s^2 + v_s^2) + \frac{1}{2} \rho_g \phi_g (u_g^2 + v_g^2) \quad (5.5)$$

The gas and solid velocities have equilibrated, due to the inclusion of drag.

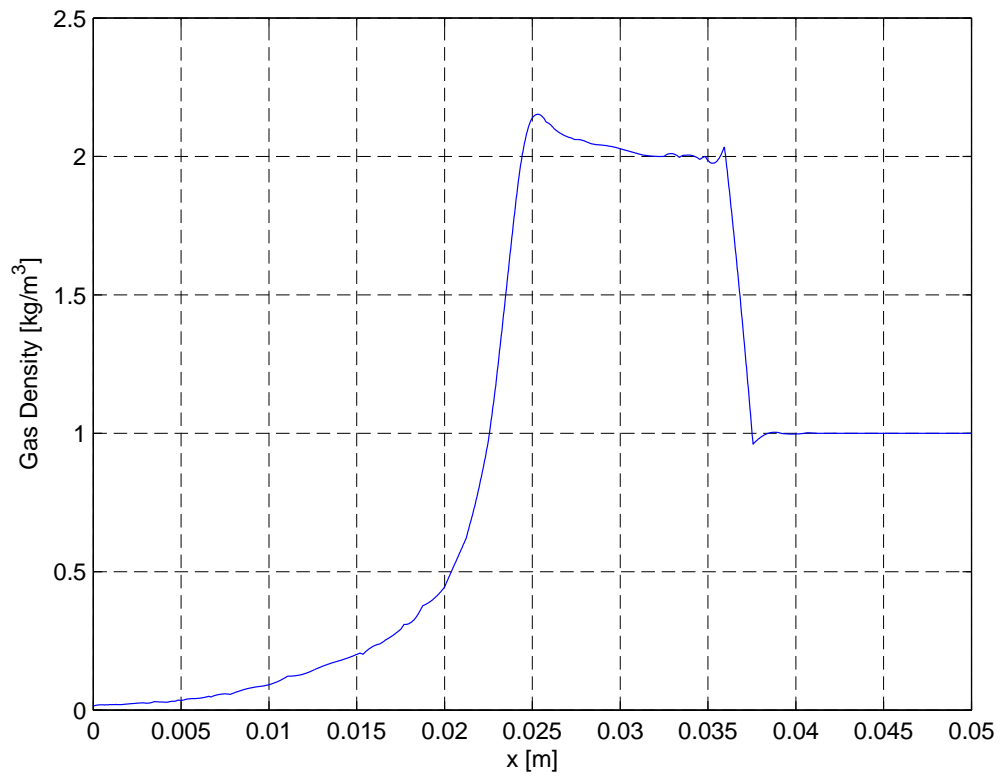


Figure 5.13. Gas density for a concentrated heat source with no-slip at $t = 50 \mu s$

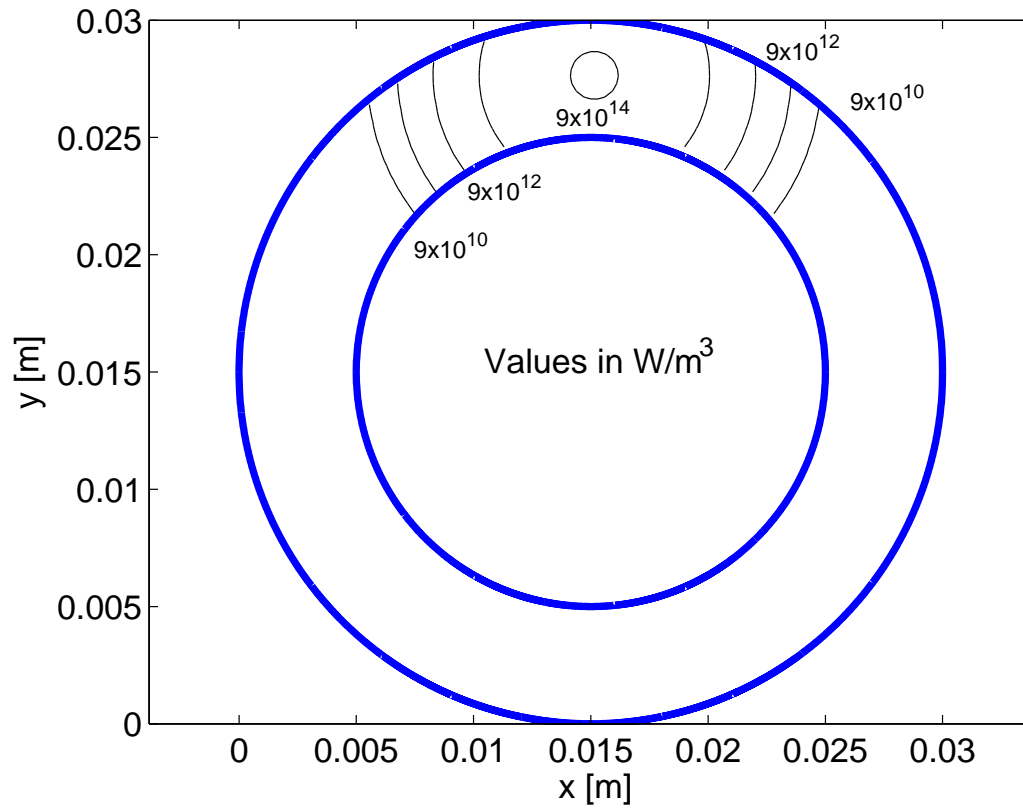


Figure 5.14. Forcing function, \mathcal{S}_e for the thin annulus

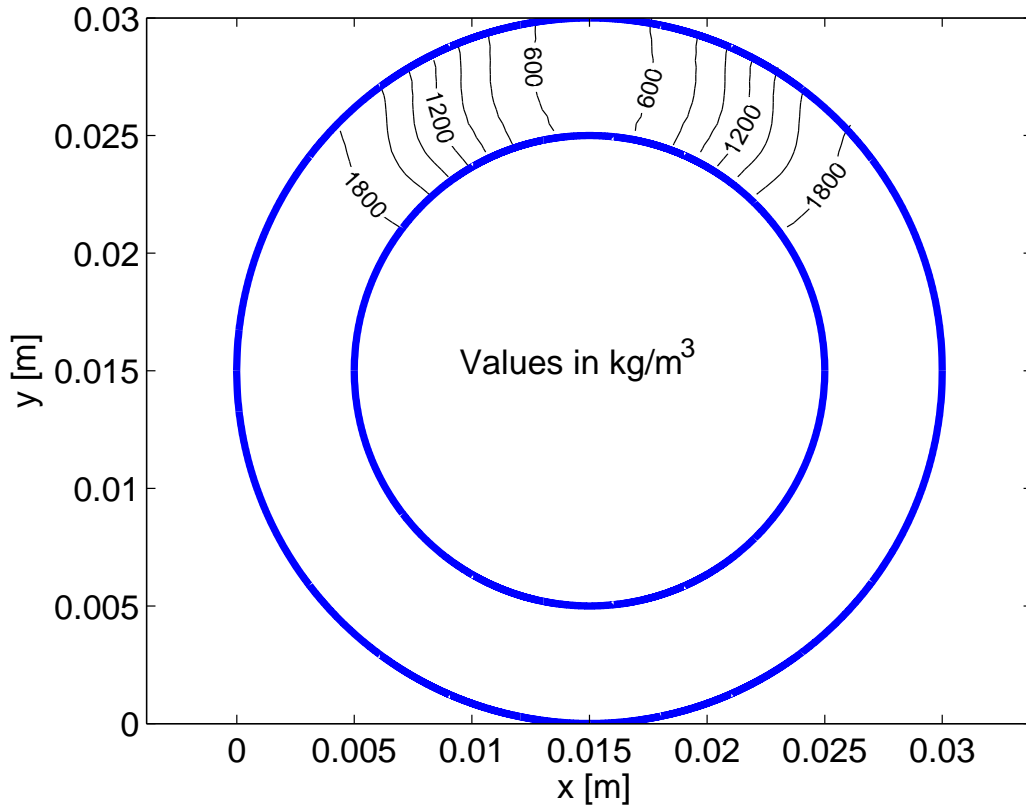


Figure 5.15. Solid density for a concentrated energy source at $t = 50 \mu\text{s}$

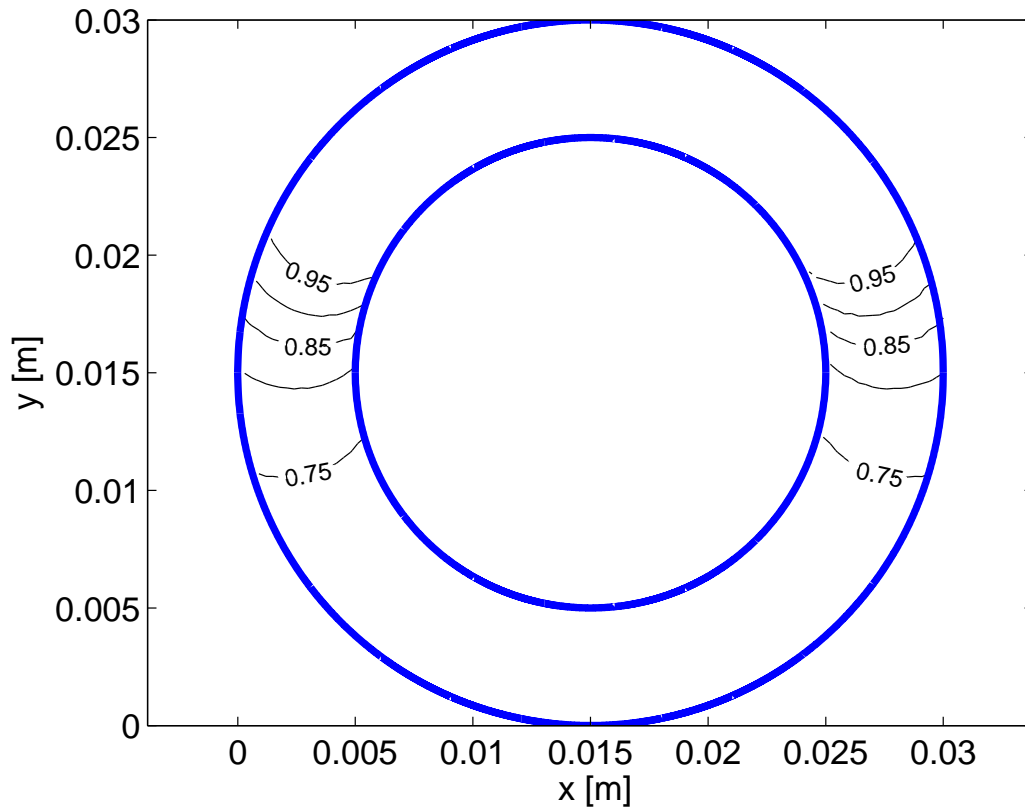


Figure 5.16. Solid volume fraction for a concentrated energy source at $t = 50 \mu s$

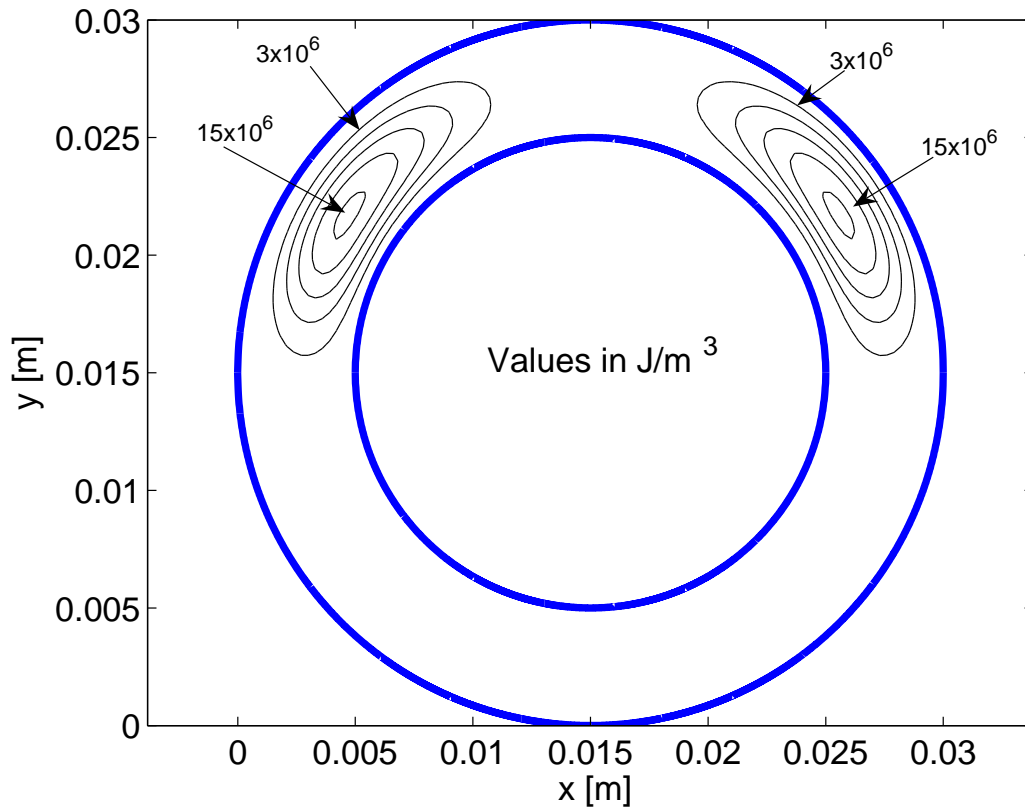


Figure 5.17. Kinetic energy for a concentrated energy source at $t = 50 \mu\text{s}$

CHAPTER 6

DISCUSSION AND FUTURE WORK

6.1 Discussion

The results shown here are an important development in compaction research, since most previous studies deal only in one-dimensional behavior. Several test problems were solved in two dimensions; unfortunately, there has been very little research done for such problems, so almost no data exist to which it is possible to compare these results. However, the one-dimensional limits of the test problems compare well with analytical and experimental results, and the two-dimensional problems show good agreement to these one-dimensional limits.

This model explicitly formulates diffusion of energy and momentum in both phases, providing the following advantages. First, such a formulation eliminates unwanted numerical problems without requiring restrictively fine meshes. Second, these results were solved using the basic solvers of commercially available software. Third, it is possible to specify a finite physical length scale which limits the physical length scales for which small scale phenomena occur, and consequently dictates the numerical length scale of the problem.

The model is well posed with initial and boundary conditions, and is converging at a uniform rate. The numerical results for a one-dimensional shock tube compare well to the analytical solution. As well, the numerical solution to the piston-driven compaction is in good agreement with experimental data. It is also apparent that

the equation set used is sufficiently general to model two-dimensional problems, since the full two-dimensional solutions compare well to the one-dimensional limits.

6.2 Future Work

There is still some question as to formulating constitutive models, such as for compaction, based on theory, rather than *ad hoc* curve fitting to experimental data. This still remains a rich field for future research. Also, it would be a straightforward extension to introduce chemical reaction into the problem by including a non-zero form of \mathcal{C} . Incorporating the current work of Lowe and Greenaway [17], which is on the effects of particle size on compaction behavior, into the full two-dimensional analysis is of particular interest to the author since the current model does not account for the physical structure of the solid matrix..

The equations presented here are general enough to allow for a fully three dimensional study of the phenomena. It would also be of interest to explore the effects of wall reflections by allowing the shocks to reach geometry edges. There are also many different forcing functions to explore, such as mass or heat sinks, fluxes of momentum or energy, and extension of one-dimensional the piston problem into more complicated geometries.

REFERENCES

- [1] H. W. Sandusky and T. P. Liddiard. Dynamic compaction of porous beds. Naval Surface Weapons Center Report 83-256, December 1985.
- [2] K. A. Gonthier and J. M. Powers. A numerical investigation of transient detonation in granulated material. *Shock Waves*, 6(4):183–195, 1996.
- [3] P. E. Luebcke, P. M. Dickson, and J. E. Field. Deflagration-to-detonation transition in granular pentaerythritol tetranitrate. *Journal of Applied Physics*, 79(7):3499–3503, 1996.
- [4] H. W. Sandusky and R. R. Bernecker. Compressive reaction in porous beds of energetic materials. Naval Surface Weapons Center Eighth Detonation Symposium, 1985.
- [5] M. R. Baer and J. W. Nunziato. A two-phase mixture theory for the deflagration-to-detonation transition (DDT) in reactive granular materials. *International Journal of Multiphase Flow*, 12(6):861–886, 1986.
- [6] H. Krier and S. S. Gokhale. Modeling of convective mode combustion through granulated propellant to predict detonation transition. *AIAA Journal*, 16(2):177–183, 1978.
- [7] P. B. Butler, M. F. Lembeck, and H. Krier. Modeling of shock development and transition to detonation initiated by burning in porous propellant beds. *Combustion and Flame*, 46(1):75–93, 1982.
- [8] J. M. Powers, D. S. Stewart, and H. Krier. Analysis of steady compaction waves in porous materials. *Journal of Applied Mechanics*, 56(15):15–24, 1989.
- [9] J. M. Powers, D. S. Stewart, and H. Krier. Theory of two-phase detonation, Part I: Modeling. *Combustion and Flame*, 80(3-4):264, 1990.
- [10] J. M. Powers, D. S. Stewart, and H. Krier. Theory of two-phase detonation, Part II: Structure. *Combustion and Flame*, 80(3-4):280, 1990.
- [11] K. A. Gonthier and J. M. Powers. A high resolution numerical method for a two-phase model of deflagration to detonation transition. *Journal of Computational Physics*, 163(2):376–433, 2000.
- [12] J. B. Bdzil, R. Menikoff, S. F. Son, A. K. Kapila, and D. S. Stewart. Two-phase modeling of deflagration-to-detonation transition in granular material: A critical examination of modeling issues. *Physics of Fluids*, 11(2):378–402, 1999.

- [13] A. K. Kapila, R. Menikoff, J. B. Bdzil, S. F. Son, and D. S. Stewart. Two-phase modeling of deflagration-to-detonation transition in granular material: Reduced equations. *Physics of Fluids*, 13(10):3002–3024, 2001.
- [14] A. Chinnayya, E. Daniel, and R. Saurel. Modeling detonation waves in heterogeneous energetic materials. *Journal of Computational Physics*, 196(2):490–538, 2004.
- [15] J. M. Powers. Two-phase viscous modeling of compaction of granular materials. *Physics of Fluids*, 16(8):2975–2990, 2004.
- [16] M. V. Papalexandris. A two-phase model for compressible granular flows based on the theory of irreversible processes. *Journal of Fluid Mechanics*, 517:103–112, 2004.
- [17] C. A. Lowe and M. W. Greenaway. Compaction processes in granular beds composed of different particle sizes. *Journal of Applied Physics*, 98(12):547, 2005.
- [18] C. A. Lowe and A. W. Longbottom. Effect of particle distribution on the compaction behavior of granular beds. *Physics of Fluids*, 18(6):066101, 2006.
- [19] K. A. Gonthier. Predictions for weak mechanical ignition of strain hardened granular explosive. *Journal of Applied Physics*, 95(7):3482–3494, 2004.
- [20] D. W. Schwendeman, C. W. Wahle, and A. K. Kapila. The Riemann problem and a high-resolution Godunov method for a model of compressible two-phase flow. *Journal of Computational Physics*, 212(2):490–526, 2006.
- [21] E. Zauderer. *Partial Differential Equations of Applied Mathematics*. Wiley, New York, 1989.
- [22] COMSOL. *FEMLAB User’s Guide and Introduction*, 2003.
- [23] A. H. Shapiro. *The Dynamics and Thermodynamics of Compressible Flow*. Kreiger, Malabar, Florida, 1953.